Chem Soc Rev

Ce3+-doped Garnet Phosphors: Composition Modification, Luminescence Properties and Applications

Journal:	*Chemical Society Reviews*
Manuscript ID	CS-REV-07-2016-000551.R2
Article Type:	Review Article
Date Submitted by the Author:	17-Oct-2016
Complete List of Authors:	Xia, Zhiguo; University of Science and Technology Beijing, School of Materials Science and Engineering Meijerink, Andries; Utrecht University,

Ce^{3+}-doped Garnet Phosphors: Composition Modification, Luminescence Properties and Applications

Zhiguo Xia[*,a], **Andries Meijerink**[*,b]

Received (in XXX, XXX) Xth XXXXXXXXX 200X, Accepted Xth XXXXXXXXX 200X
DOI: 10.1039/b000000x

Garnets have a general formula of $A_3B_2C_3O_{12}$ and form a wide range of inorganic compounds, occurring both naturally (gemstones) and synthetically. Their physical and chemical properties are closely related to the structure and composition. Especially Ce^{3+}-doped garnet phosphors have a long history and are widely applied, ranging from flying spot camera, lasers and phosphors in fluorescent tubes to more recent applications in white light LEDs, afterglow materials and scintillators for medical imaging. Garnet phosphors are unique in their tunability of the luminescence properties through variations in the {A}, [B] and (C) cation sublattice. The flexibility in phosphor composition and the tunable luminescence properties rely on design and synthesis strategies for new garnet compositions with tailor-made luminescence properties. It is the aim of this review to discuss the variation in luminescence properties of Ce^{3+}-doped garnet materials in relation to the applications. This review will provide insight in the relation between crystal chemistry and luminescence for the important class of Ce^{3+}-doped garnet phosphors. It will summarize previous research on the structural design and optical properties of garnet phosphors and also discuss future research opportunities in this field.

[a] *The Beijing Municipal Key Laboratory of New Energy Materials and Technologies, School of Materials Sciences and Engineering, University of Science and Technology Beijing, Beijing 100083, China. E-mail: xiazg@ustb.edu.cn . Fax: +86-10-8237-7955;Tel: +86-10-8237-7955*

[b] *Condensed Matter and Interfaces, Debye Institute for Nanomaterials Science, Utrecht University, Princetonplein 5, 3584 CC Utrecht, The Netherlands. E-mail: a.meijerink@uu.nl . Tel.: +030-2532202. Fax: +030-2532403.*

Zhiguo Xia (37) is a professor of materials chemistry and physics at University of Science and Technology Beijing (USTB). He obtained his bachelor (in 2002) and master (in 2005) degrees (both in Applied Chemistry) from Beijing Technology and Business University (BTBU), and he received his PhD degree (Inorganic Chemistry) from Tsinghua University (Beijing, China) in 2008. Since then he has been working as an assistant and associate Professor in China University of Geosciences, Beijing (CUGB), 2008-2014. After that, he joined USTB as a full professor. His research interests focus on inorganic solid state chemistry and new solid state functional materials, and his recent work involves the designing of new rare earth phosphors for white LED by integrating structural discovery, modification and structure-property relation studies.


(Zhiguo Xia)


(Andries Meijerink)

Professor Andries Meijerink (52) received his PhD degree in Chemistry (Cum Laude) in the group of Prof. George Blasse, 1990 at Utrecht University, The Netherlands. After a post-doctoral period in the group of Prof. John Wright at the University of Wisconsin in Madison he returned to The Netherlands where, at the age of 32, he was appointed at the chair of Solid State Chemistry in the Debye Institute of Utrecht University. He leads an active research group that focuses on the optical spectroscopy of lanthanide ions in solids and of nanocrystalline semiconductor quantum dots. In the field of lanthanide ions his recent work involves fundamental research on finding new concepts also related to applications in solar cells, LEDs and scintillators. For his research on phosphors he has received various (inter)national prizes. Since 2009 he is a member of the Royal Dutch Academy of Sciences in The Netherlands.

1. Introduction

1.1 Ce^{3+}-doped garnet phosphor: history and applications

Yttrium aluminum garnet ($Y_3Al_5O_{12}$ or YAG) and its compositional derivatives doped with Ce^{3+} form a class of highly efficient luminescent materials (phosphors) with a remarkably rich history of applications ranging from cathode ray phosphors and color correction phosphors in fluorescent tubes to more recent application as scintillator, afterglow material and as color converter in white light-emitting diodes (LEDs).[1-8] YAG can be regarded as a typical example of the garnet structure possessing a cubic structure with *Ia*3*d* symmetry (Fig. 1). Even though the structure is cubic, the unit cell is not simple. The general formula for a perfect garnet is $\{A\}_3[B]_2(C)_3O_{12}$ where A, B and C are cations in different symmetry sites. The garnet structure can be described in terms of a 160 atom body-centered cubic unit cell. In this unit cell, depicted in Fig. 1, the A atoms occupy 24 (c) sites of 8-fold dodecahedral coordination, the B atoms are in 16 (a) sites with 6-fold octahedral coordination and C atoms occupy 24 (d) sites with 4-fold tetrahedral coordination.[1, 9] Each octahedron is connected to six tetrahedrons while each tetrahedron is connected to four $[AlO_6]$ octahedrons by sharing corners. It is the presence of the three different cation sites that give Ce^{3+}-doped garnets their remarkable flexibility in tuning and optimization of the luminescence properties for specific applications through cation substitution.

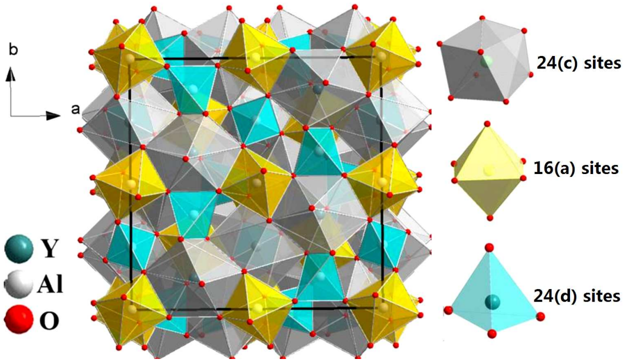

Fig. 1 Schematic of the crystal structure of garnet-type $Y_3Al_5O_{12}$ and the coordination atoms of polyhedrons for different sites, 24 (c) sites of $[YO_8]$, 16 (a) sites of $[AlO_6]$ and 24 (d) sites of $[AlO_4]$.

The history of garnets dates back to the Bronze age. Garnets have been used for thousands of years as abrasives, because of their hardness, and as gemstones, related to their high refractive index and beautiful coloring through incorporation of transition metal ions on the tetrahedral or octahedral sites. The English word Garnet originates from the Latin "Granatum", which means many grains and is related to the pomegranate fruit, having many red seeds that resemble some of the dark red garnet gemstones in structure and color.

The scientific history of garnet-type compounds begins in 1928 when Menzer assigned the garnet structure to the space group *Ia*3*d*.[10] In 1967, Blasse and Bril were the first to report on Ce^{3+}-doped YAG (YAG:Ce^{3+}) as a new phosphor for flying-spot cathode ray tubes (CRT).[1] The observation of yellow emission from Ce^{3+} was remarkable as usually ultraviolet (UV) or blue emission is observed for Ce^{3+}. The bright yellow emission for Ce^{3+} in YAG was explained by a strong crystal field splitting but even today the reason for the low energy of the emitting the 5*d* state of Ce^{3+} in garnets is not completely understood. The unique combination of a short lived (*ns* decay time) efficient yellow emission combined with strong absorption in the blue spectral region has been the basis of the many applications of Ce^{3+}-doped garnets. The strong absorption in the blue gives YAG:Ce^{3+} its characteristic yellow body color. Following the application as CRT phosphor and for fast electron detection in scanning electron microscopes, Van Kemenade et al. described the application of YAG:Ce^{3+} in low-pressure mercury vapor discharge lamps for color conversion of blue emission from the mercury discharge to yellow light.[11] In the 1990s, YAG:Ce^{3+} and LuAG:Ce^{3+} (($Lu_3Al_5O_{12}$:Ce^{3+}) were proposed as fast and efficient scintillator materials.[12, 13] Single crystalline disks of YAG:Ce^{3+} were used to monitor and control the dose of VUV radiation in wafer steppers. The biggest commercial application is more recent. The discovery of the blue LED has revolutionized the lighting market as was recognized by awarding the 2014 Nobel Prize in physics for the development of the blue LED.[14] Solid-state lighting plays a vital role in the lighting and display industries and will continue to create value in the future.[15, 16] Following the discovery of the blue LED, the possibility for white LEDs (*w*-LEDs) was pioneered at Nichia Chemical Company and the first *w*-LEDs became commercially available in 1997.[17] For conversion of the blue LED emission the yellow light emitting YAG:Ce^{3+} phosphor was selected in combination with 460 nm blue-emitting InGaN LED chips. Till now, YAG:Ce^{3+} is the most widely applied phosphor in *w*-LEDs.[18-22]

Garnets possess a cubic crystal structure but with a complex arrangement of different cations in the unit cell. Because of this the garnet phosphors are unique in their tunability of the luminescence properties through variations in the {A}, [B] and (C) cation sublattice. The dodecahedral A site can be occupied by rare earth ions, such as Y^{3+}, Lu^{3+}, Gd^{3+}, Tb^{3+} or La^{3+} ions, or divalent cations, such as Ca^{2+}; the octahedral B site can be occupied by Al^{3+}, Ga^{3+}, Sc^{3+}, Sb^{3+}, In^{3+}, and even ions with a different charge such as Mg^{2+} or Mn^{2+} while the tetrahedral C site is typically occupied by Ga^{3+} or Al^{3+}, but can also contain differently charged ions as Si^{4+}, Ge^{4+} or Mn^{2+} while maintaining the garnet crystal structure, and many other substitutions are also possible.[4, 23] The very wide range of solid solution compositional variation enables tuning and optimization of optical properties in relation to specific applications. The Ce^{3+} emission color can be tuned from the green to the orange-red spectral region through variation in the crystal field splitting and the nephelauxetic effect (see section 1.2 for a detailed description of these effects). Therefore, Ce^{3+}-doped garnet phosphors possess a long and rich history on structure modification and luminescence studies.

Garnet-based Ce^{3+} phosphors have been used for a wide variety of applications in different fields.[18-22] This makes the Ce^{3+}-doped garnets unique. Fig. 2 presents some typical applications of Ce^{3+}-doped garnet phosphors, including but not limited to: indoor and outdoor lighting, backlights in displays, solid-state lasers, flying-spot scanning, traffic lights, automobile lights, plasma display panel devices, afterglow materials, dye industry, scintillators for medical imaging and homeland security, transparent ceramics, and so on. Table 1 summarizes some important Ce^{3+}-doped garnet phosphors including their chemical composition, photoluminescence emission (PL) and excitation (PLE) wavelength and their corresponding applications.[24-54] More details on the garnet phosphors mentioned and the background to understand the preparation method, variation in luminescence characteristics and their application can be found in the following sections and the corresponding references.[55-59]

Table 1 Properties and applications of some typical Ce^{3+}-doped garnet phosphors. In addition to the chemical composition, the position of the excitation and emission band corresponding to transitions between the 4*f* ground state and the lowest energy 5*d* state are given.

Application	Chemical composition	λ_{ex} (nm)	λ_{em} (nm)	Ref.
w-LED Phosphors	$Y_3Al_5O_{12}:Ce^{3+}$	470	532	1
	$Lu_3Al_5O_{12}:Ce^{3+}$	440	505	24
	$Ca_3Sc_2Si_3O_{12}:Ce^{3+}$	455	505	26, 27
	$Tb_3Al_5O_{12}:Ce^{3+}$	470	553, 620	28, 29
	$Y_3Al_4GaO_{12}:Ce^{3+}$	450	519	30
	$Y_3Sb_2Al_3O_{12}:Ce^{3+}$	465	528	31
	$Y_3Al_{5-x}Si_xO_{12-x}N_x:Ce^{3+}$ (x=0.1)	470	620-630	32, 33
	$Y_3Mg_2AlSi_2O_{12}:Ce^{3+}$	440	600	34-36
	$CaLu_2Mg_2(Si,Ge)_3\ O_{12}:Ce^{3+}$	470	605	37, 38
	$CaLu_2Al_4SiO_{12}:Ce^{3+}$	450	510-530	39
	$Mg_3Y_2Ge_3O_{12}:Ce^{3+}$	466	555	4, 40
	$MgY_2Al_4SiO_{12}:Ce^{3+}$	452	566	41
	$Lu_3(Al,Mg)_2(Al,Si)_3O_{12}:Ce^{3+}$	450-462	542~571	42
	$Ca_2GdZr_2(AlO_4)_3:Ce^{3+}$	417	500	43
	$Ca_2LaZr_2Ga_3O_{12}:Ce^{3+}$	430	515	44
	$Ca_3Hf_2SiAl_2O_{12}:Ce^{3+}$	400	508	45
Scintillators	$Lu_3Al_5O_{12}:Ce^{3+}$	440	505	46, 47
	$Tb_{2.2}Lu_{0.8}Al_5O_{12}:Ce^{3+}$	459	565	48
	$(Lu,Gd)_3(Ga,Al)_5O_{12}:Ce^{3+}$	345	530	49
	$Gd_3(Al,Ga)_5O_{12}:Ce^{3+}$	445	540-565	50
Afterglow Phosphors	$Y_3Sc_2Ga_3O_{12}:Ce^{3+}$	440	500	51
	$Y_3Sc_2Ga_{3-x}Al_xO_{12}:Ce^{3+}$	414	503	52
	$Mg_3Y_2(Ge_{1-x}Si_x)_3O_{12}:Ce^{3+}$	455	580~595	53

Fig. 2 Some representative application fields of Ce^{3+}-doped garnet phosphors including white light LEDs, scintillators, afterglow materials, laser crystals, and their corresponding applications.

In the various applications of the Ce^{3+}-doped garnets shown in Fig. 2, different properties are important and require optimization. To be able to appreciate the following Sections in which the tuning of the optical properties of Ce^{3+}-doped garnets is reviewed in relation to the various applications, it is good to provide a brief description of the different applications of the phosphors and the requirements that are important in each of these.

In the first publication on $YAG:Ce^{3+}$ from 1967 by Blasse the potential application in a flying spot camera was mentioned. A flying spot camera uses a monochrome CRT. The luminescent material applied in dots or bars (pixels) on the inside of the glass tube is excited by a high energy electron beam (20-50 keV electrons) that scans the inside of the glass CRT (see Fig. 3). The high energy of the electrons is converted into light (cathode luminescence) by the phosphor and a 2D image is written by a rapid scan of all phosphor pixels. In a flying spot camera a short luminescence decay time is required to allow for a high image capture rate. The short ns life time of the Ce^{3+} emission in $YAG:Ce^{3+}$ is particularly advantageous for this application. In a conventional color television, a CRT with three different ~100 µm sized bars or dots with a red, green and blue emitting phosphor are used for each pixel. The energy of the fast electrons is converted into blue, green or red light by the phosphors in each pixel and a color image is obtained. Operating parameters for CRT phosphors involve:

- Efficient excitation by electron beams
- Stability under high energy electron excitation
- No afterglow to prevent ghost images
- Operating temperature below 50 °C
- Vacuum tube protects against moisture

A challenge for the performance of $YAG:Ce^{3+}$ in CRT applications were afterglow problems. Even though the radiative decay rate of the yellow Ce^{3+} *d-f* emission is short (60-70 ns) the presence of defects results in afterglow related to defects in the garnet host and extensive studies on defects and traps in $YAG:Ce^{3+}$ were conducted in the 1970s.[60, 61]

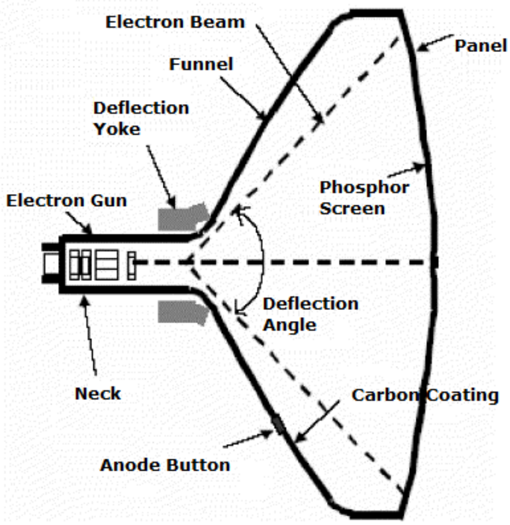

Fig. 3 Schematic of a cathode ray tube. An electron gun emits electrons that are accelerated over 30-50 kV. The high energy electron beam is deflected by two sets of electromagnets for horizontal and vertical steering of the beam to scan every pixel with a phosphor (e.g. $YAG:Ce^{3+}$) converting the energy of the high energy electrons to visible light. By varying the intensity of the exciting beam for every point on the screen an image is written that can observed through the glass. (Reprinted with permission from ref. 62, copyright 2007, Elsevier.)

The second commercial application $YAG:Ce^{3+}$ was as color converter in compact fluorescent tubes (CFLs) and dates back to the 1980s.[11] In a (compact) fluorescent tube a low pressure mercury discharge produces UV radiation, mainly at 254 nm, but also some vacuum ultraviolet (VUV) radiation (185 nm) and a small portion of blue (436 nm) light are emitted. Conversion of the UV radiation into blue, green and red light by a blend of three phosphors (typically $BaMgAl_{10}O_{17}:Eu^{2+}$ for blue, $LaPO_4:Ce^{3+},Tb^{3+}$ for green and $Y_2O_3:Eu^{3+}$ for red) coated on the inside of the glass tube produces white light. However, in CFLs the relative fraction of blue 436 nm light is higher than in linear tubes and too high to make warm white light. To solve this problem YAG:Ce^{3+} was added to the phosphor blend to absorb part of the 436 nm light and convert this to yellow. The red, green and blue phosphors in fluorescent tubes absorb UV radiation but not the blue 436 nm mercury line. Conditions for phosphors in fluorescent tubes are:

- Efficient excitation by mercury lines (mainly 254 nm)
- Relative low excitation density (large phosphor area)
- Operating temperatures typically around 50 °C
- Chemical stability against reaction with mercury gas
- Long term stability (typical operating time 10 000 h)
- Sealed glass tube protects against moisture.

Application of YAG:Ce^{3+} as a color converter in specialty CFLs was a niche application and did serve to improve the color temperature of deluxe CFL lamps.

In the 1990s extensive research started on Ce^{3+}-doped garnets for application as a scintillator material. Medical x-ray imaging techniques like conventional x-ray imaging (with intensifying screens) and advanced techniques like CT (computed tomography) and PET (positron emission tomography) rely on luminescent materials that convert x-rays transmitted by the patient/object that is imaged into light for detection by photographic film, charge coupled devices or fast photodetectors. Requirements for x-ray phosphors depend on the specific imaging technique and include:

- High density for efficient absorption of x-rays
- High efficiency of conversion x-ray photons into light
- No afterglow (to prevent ghost images)
- Operating temperature below 50 °C
- Short luminescence life time (especially for PET)
- Radiation stable
- Transparent (for PET, high energy physics)

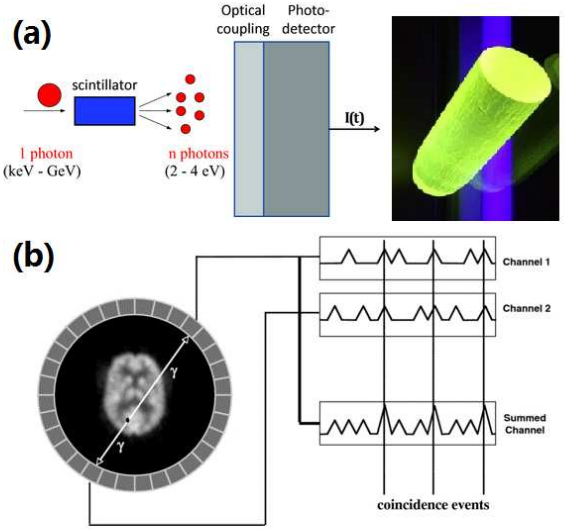

Fig. 4 (a) Operating principle of a scintillator converting one high energy x-ray photon into a large number of lower energy visible photons that are detected by a photodetector (Reproduced with permission from Ref. 63, copyright 2015, Wiley.), and the photograph of a LuAG:Ce^{3+} scintillator crystal showing green Ce^{3+} emission under UV-excitation (Reproduced with permission from ref. 64, copyright 2013, Elsevier.), (b) Schematic of PET scanner with a patient surrounded by a ring of scintillator crystals and photodetectors for coincident detection of two 512 keV photons emitted at a 180° angle in positron annihilation events (Reprinted with permission from ref. 65, copyright 2008, IOP Publishing.).

In Fig. 4 medical imaging using a scintillator is illustrated. The short ns emission life time of the Ce^{3+} *d-f* emission is particularly suitable for PET which relies on the simultaneous detection of two 512 keV γ-rays that are emitted under a 180° angle following electron-positron annihilation. The shorter the response time of detection, the higher will be the accuracy with which location of the positron emitter can be determined. The density of YAG is 4.56 g/cm^2 and the performance as a scintillator by increasing the density (and thus the stopping power for x-rays) to 6.73 g/cm^2 for LuAG by replacing the lighter Y^{3+} by the heavier Lu^{3+}.

The cubic crystal structure of garnets is beneficial for making transparent scintillator crystals which are used in PET and also in x-ray and γ-ray detectors in high energy physics. Because of the isotropic refractive index for cubic materials transparent ceramics can be formed by pressing micro or nanocrystalline precursor material.[66-68] The transparent ceramics have lower cost and higher mechanical strength compared to single crystals.

The final and by far the biggest commercial application of YAG:Ce^{3+} is in white light LEDs. The field of *w*-LEDs started with the discovery of the blue (In,Ga)N LED in 1993.[14] Before that only longer wavelengths (IR, red, green) LEDs existed with reasonable efficiency. With the discovery of blue (In,Ga)N LEDs it became possible to generate white light with LEDs. Blue, green and red LEDs were combined which made it possible to generate LED based white light but color stability and reproducibility were hard to realize. Next, researchers started considering making white light by placing luminescent materials directly on top of the blue LED. Partial conversion of blue light to red and green or yellow/orange yields white light (see Fig. 5). The operating conditions for LED phosphors are challenging. In addition to efficient conversion of blue light from the LED chip into longer wavelength green and red or yellow/orange light, the LED-specific conditions include:

- Long term stability under extreme excitation densities
- High temperature stability of material and luminescence (phosphor temperature can reach 100-200 °C).
- Small thermal shift of the emission maximum
- Short emission life time to prevent saturation
- Chemical stability (against moisture at high T)

The small area of the blue (In,Ga)N chip (<1 mm^2) results in very high excitation densities. For a 1 W LED the excitation density can exceed 10^5 W/cm^2, which is 100-1000 times higher than for other applications discussed while typical operating times are 30 000 h or more. In 1996 YAG:Ce^{3+} was discovered as *w*-LED phosphor and a year later the first commercial YAG:Ce^{3+} based *w*-LEDs were introduced.[17] Still, today YAG:Ce^{3+} is the most widely applied *w*-LED phosphor and the yellow-colored YAG:Ce^{3+} powder can be observed in e.g. *w*-LEDs in mobile phones flashlights (see Fig. 2).

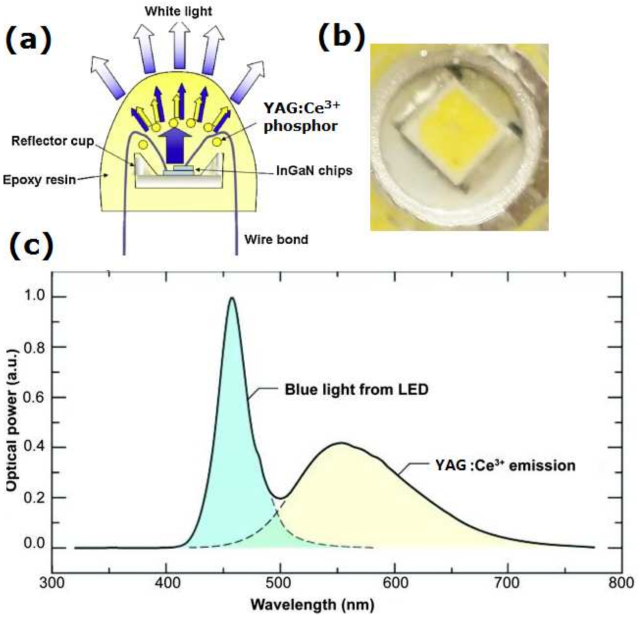

Fig. 5 (a) Schematic of a w-LED. Blue emission from a (In,Ga)N LED is partially absorbed and converted to yellow emission by a thin layer of YAG:Ce^{3+} phosphor applied on top. (Reproduced with permission from ref. 8, copyright 2010, Elsevier.). (b) The yellow phosphor can be observed in the close-up picture of a *w*-LED flashlight. (c) The emission spectrum showing the transmitted blue light and phosphor converted yellow light result in white light. (Reproduced with permission from ref. 69, copyright 2014, Wiley.).

Combining blue diode emission and yellow emission from YAG:Ce^{3+} gives rise to rather cold white light. To improve the color temperature and make a warmer white LED, orange or red emitting phosphor can be added. In Fig. 6 the black curve marks the color temperature as defined by the position of a black body radiator with a specific temperature. Red shifting the Ce^{3+} emission will result in a shift to the right on the black body locus (warmer white). In garnets cation substitution is used to shift the emission spectrum and will be discussed in this review. In addition, a large variety of alternative (non-garnet) LED phosphors have been developed and are applied in *w*-LEDs, often in combination with YAG:Ce^{3+} to change the color temperature as well as to improve the color rendering. The color rendering index reflects how well colors are reproduced in comparison to colors perceived in sunlight. A broader emission spectrum, including the red spectral region, will give superior color rendering.

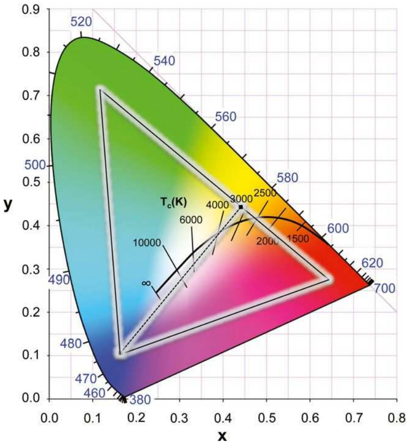

Fig. 6 CIE chromaticity diagram which quantifies emission colors of light sources in x, y coordinates. The outside line marks saturated (monochromatic) colors in the visible region (380-700 nm). For any emission spectrum the color coordinates x and y can be calculated. The central black line shows the black body curve representing the *x*, *y* coordinates of a black body radiator with temperatures indicated. The line is situated in the central region of the diagram that corresponds to white light. Higher temperatures shift the spectrum to the blue (cool white). The triangle marks the color gamut required in color displays that is obtained by using three phosphors with color coordinates at the corners of the triangle. The dotted line between the blue and yellow saturated colors demonstrates how white is obtained by mixing blue and yellow emission in the correct ratio. Reproduced with permission from ref. 69, copyright 2014, Wiley.).

1.2 Luminescence theory of Ce^{3+} in garnet phosphors

Luminescence is the phenomenon, in which an ion, molecule or atom returns to the ground state by spontaneous emission of photons after they are promoted into excited states by absorbing photons of appropriate energy. Only a limited number of elements have been used as optically active centers in luminescent materials (also known as phosphors). The largest group of luminescent centers applied in light emitting materials for technological applications are the rare earth ions, which comprises the group lanthanides, yttrium and scandium.[70-73] The series of lanthanides (Ln) is situated at the bottom of the periodic table and it is the group of elements for which the inner 4*f* shell is filled with electrons. The most stable valence state is 3+ and the electron configuration of the Ln^{3+} ions is $4f^n5s^25p^6$, where *n* is the number of electrons in the 4*f* inner shell and can vary from 0 (empty 4*f* shell) to 14 (4*f* shell completely filled). The Ce^{3+} ion has the simplest electron configuration among the luminescent rare earth ions with one 4*f* electron: $4f^1$. The luminescence properties of Ce^{3+} result from optical transitions between the $4f^1$ ground state and the $5d^1$ excited state. The $4f^1$ ground-state configuration splits into two sublevels, $^2F_{5/2}$ and $^2F_{7/2}$, and these two sublevels are separated by about 2,000 cm^{-1} as a result of spin-orbit coupling. This is the reason for the double structure usually observed in the Ce^{3+} emission band. The $5d^1$ excited state configuration is split into two to five components by the crystal field. The number of 5*d* levels depends on the crystal field symmetry.

The crystal field splitting of the 5*d* levels of Ce^{3+} ion in different coordination has been extensively investigated,[74-79] also based on the spectroscopic data for lanthanide activated garnets $RE_3Al_5O_{12}$ (RE = Gd, Y, Lu).[80] Ce^{3+}-doped compounds generally show 5*d*-4*f* emission in the near UV, but in case of high crystal field splitting, such as in garnets, visible emission is sometimes observed. Since garnet structure compounds are stable from a chemical and photochemical points of view, phosphors possessing garnet crystal structure generally show a high stability. Moreover, the garnet crystal structure generates a strong crystal field strength on the dodecahedral site where the Ce^{3+} ions are incorporated and therefore, the *d*-*f* emission is shifted to the green,[26-29, 81] yellow[1], or even orange-red[37-39] spectral region depending on the lattice composition.

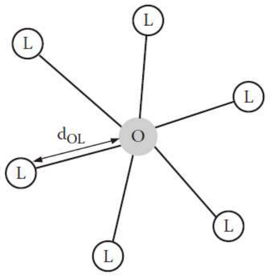

Fig. 7 An optically active center, OL_6, containing a doping ion O that is coordinated to six ligand ions L. (Reprinted with permission from ref. 82, copyright 2005, Wiley.)

The most important effects on Ce^{3+} and the interaction with a host lattice are the crystal field splitting and the nephelauxetic effect. To understand these effects we consider the optically active dopant (cat)ion and its neighboring (an)ions also called ligands. Fig. 7 gives a scheme of a luminescence center consisting of a dopant ion O coordinated to six ligand ions L. Typically as an example the octahedral six-coordinated center, OL_6, is considered and this is also called the optically active center as the optical transitions are localized on the central ion O and the surrounding ligands L. For a given dopant ion, the absorption and emission properties are significantly affected by the host lattice. This is because the energy level structure of a free ion O is altered by interaction with the nearest neighboring ions L in the lattice by the nature of chemical bonds between O and L (i.e., covalency, bond length, coordination number, symmetry, etc.).[82, 83] Here we will focus on the luminescence center Ce^{3+} in the 24 (c) sites of 8-fold coordination for the garnet structure but the same principles as for the OL_6 center apply. The Ce^{3+} emission is strongly affected by the host lattice through interaction with the ligands. As was mentioned, the electronic energy levels of an activator ion in a crystal differ greatly from those of a free ion.[84] For example, the difference in energy between the 5*d* and 4*f* levels of gaseous (free) Ce^{3+} ions is in the high energy UV region (~200 nm, 50 000 cm^{-1}), whereas for Ce^{3+} ions in a crystal, this energy difference can range from UV to the lower energy visible region, depending on the host crystal.[78]

When an activator ion is placed in a host crystal, two major effects dictate the photoluminescence properties: the centroid shift (determined by the so-called nephelauxetic effect) and the crystal field splitting of the 5*d* orbital. Both effects will contribute to a decrease in the energy difference between the lowest 5*d* level and the 4*f* ground state, which is referred to as the redshift. The two effects mentioned above are illustrated for Ce^{3+} in Fig. 8a, with the total redshift is labeled *D*. Both the crystal field and nephelauxetic effect influence the energy for the electron in the 5*d* orbitals of the activator ion, whereas the well-shielded 4*f* states are not strongly affected. The position of the 5*d* levels can change by tens of thousands of wave numbers from one compound to another. The centroid shift is a lowering in average energy of all the 5*d* levels of the activator ion and is caused by a decrease in the inter-electron repulsion. The centroid shift can be determined from the position of all 5*d* levels and is defined as the (degeneracy weighted) average energy of all 5*d* levels. This average energy is known as the bary center. The centroid shift increases with increasing covalency of the bond between the Ce^{3+} ion and the surrounding anions, i.e. with increasing polarizability and decreasing average anion electronegativity with as a general trend a lowering of the energy going from F^- to O^{2-} to N^{3-} or S^{2-} ligand coordination of Ce^{3+}. The series of anions in which the centroid shift increases is known as the nephelauxetic series. As the degree of covalency in bonding between the activator ion and surrounding anions increases, the energy for an electron in the 5*d* orbital is reduced due to stabilizing effects of the covalent bond. The name 'nephelauxetic' originates from the Greek for 'cloud expanding' which referring to increased delocalization (expansion) of the dopant *d* orbital ('electron cloud') as a result of increased covalency.

The second effect, crystal field splitting, is the difference in energy between the highest and lowest 5*d* levels and is again an effect of the host crystal. The magnitude of crystal field splitting depends on the bond lengths from the activator ion to the coordinating anions, the molecular orbital overlap or degree of covalency between the activator ion and its ligands, the coordination environment, and the symmetry of the activator site. For a simple point charge model it has been derived that the crystal field splitting for varies with the distance between the central cation and the ligands as[80, 85]

$$Dq = \frac{ze^2r^4}{6R^5} \qquad (1)$$

In the above equation, *Dq* is measure of the crystal field strength, *R* is the distance between the central ion and its ligands (equivalent to d_{OL} in Fig. 7), *z* is the charge or valence of the coordinating anions, *e* is the charge of an electron, and *r* is the radius of the *d* wave function. For an octahedral coordination the crystal field splitting is 10 D_q, as given in Fig. 8a. As the bond length, or polyhedral volume, increases the crystal field splitting decreases. The crystal field splitting tends to be largest for octahedral coordination, followed by cubic coordination and dodecahedral coordination.[80] Furthermore, distortion of the activator ion site may affect crystal field splitting.[4] In fact, in the garnet structure the distortion from cubic symmetry is important in explaining the unusually long wavelength for the Ce^{3+} ion (*vide infra*).

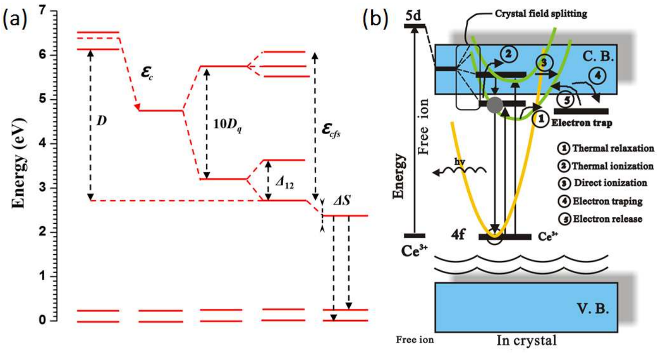

Fig. 8 (a) Energy level structure of Ce^{3+} showing the depression *D* of the lowest 5d level with respect to the free ion energy levels of Ce^{3+}. Covalency (nephelauxetic effect) gives rise to a centroid shift ε_c of the degeneracy weighted average 5*d* energy (known as the bary center). The crystal field splitting of the 5*d* state gives rise to a further red shift of the emitting lowest energy 5*d* state. In addition to the 10*Dq* splitting by the cubic crystal field there is an additional splitting Δ_{12} of the lower e_g and also a splitting of the higher t_{2g} state because of a tetragonal distortion for Ce^{3+} in garnets. Finally, there is a small additional red shift of the emission due to the Stokes' shift ΔS; (b) Schematic model of two thermal quenching mechanisms of the Ce^{3+} emission by (1) cross-over to the ground state parabola or (2) electron transfer to the CB from 5*d* levels in or close to the CB. (Reprinted with permission from ref. 86, copyright 2013, Elsevier.).

The luminescence of Ce^{3+} has been extensively studied in garnet structure. Substitution of a constituent element of the host crystal by another element of different ionic radius will increase or decrease the lattice constants of the host crystal and change the ligand coordination parameters while differences in the chemical nature can affect the covalency of the bonds as well as the positions of the valence band (VB) and conduction band (CB) edges of the host. These changes will influence the crystal field splitting for the activator, will cause a spectral shift in the Ce^{3+} luminescence and can influence the thermal quenching behavior of the luminescence. Because of shielding by the outer $5s$ and $5p$ electrons, the energy level structure for the $4f$ ground state of Ce^{3+} is fairly insensitive to host and crystal field effects and is depicted as two levels separated by ~2000 cm^{-1}.

The Ce^{3+} emission usually varies from the ultraviolet to the blue spectral region in fluorides and oxides. In covalent and strong crystal field surroundings, the $5d$ orbital shifts to lower energies, resulting in yellow and even red emission colors of Ce^{3+} as has been observed for Ce^{3+} in sulfides and nitrides.[86-89] Crystal field splitting generates two to five 5d components depending on the site symmetry of the site in the host lattice where Ce^{3+} is incorporated. In cubic symmetry the 5d state splits in two levels (e_g and t_{2g}) that will split further for deviations from cubic symmetry. The unique long wavelength emission (green-yellow-orange) for Ce^{3+} in garnets is, although not fully understood, ascribed to an additional splitting Δ_{12} of the e_g crystal field component. The crystal field splitting for Ce^{3+} is schematically depicted in Fig. 8(a). The additional splitting of the e_g state results in a lower energy $5d_1$ level and a higher energy $5d_2$ level separated by ~1 eV (8000 cm^{-1}). It is because of this large splitting that the emission from the lowest energy $5d_1$ state is in the green-yellow-orange spectral region. The larger the distortion from cubic symmetry, the more the emission shifts to lower energies.

An important mechanism to tune the Ce^{3+} emission wavelength is through changes in Δ_{12} by varying the distortion of the cubic coordination. In this way, both the excitation and emission energies can be tuned through variations in the host crystal composition and structure. As mentioned above, the garnet host lattice offers great flexibility by the substitutions in the A, B or C cation sites for the perfect garnet structure of $\{A\}_3[B]_2(C)_3O_{12}$. Because these cation sites can be substituted by various types of ions, a wide range of garnet solid solutions can be formed with varying centroid-shifts and crystal field strengths for the Ce^{3+} ion.[21, 79] Mostly it is observed that the crystal field splitting decreases when the ionic radius increases for the host cation for which the optically active ion substitutes. A larger cation site comes with a larger cation-ligand distance, reducing Dq, as shown in (1). However, for Ce^{3+} in garnets it has been shown that when the radius of the host cation on the dodecahedral site increases the crystal field splitting also increases and the emission of Ce^{3+} shifts to longer wavelengths. On the other hand, the increased radius of ions occupying tetrahedral and/or octahedral sites leads to emission shift towards shorter wavelengths. This is because of the large influence of the splitting Δ_{12} on the emission wavelength. The Δ_{12} splitting is not necessarily related to the ion-ligand distance but more affected by the distortion from cubic symmetry which explains the sometimes counter intuitive trends of host cation substitution on the $5d$-$4f$ emission wavelength. In the next section this will be extensively discussed with a large variety of cation substitutions. In the final section on modelling it will be shown that theoretical calculations point to a role of electronic effects to explain the increase in crystal field splitting upon substitution with larger cations on the dodecahedral site.

We can see from Fig. 8a that the emission wavelength depends on both the overall $4f$–$5d$ separation and the crystal field splitting of the d-levels. The $4f$-$5d$ separation is approximately constant for some specified systems and the crystal field effect plays an important role in shifting the emission. The compositional substitution influences not only the crystal field strength but also the electronic band structure of the garnet host. Therefore, the relative energies of the $5d$ levels of Ce^{3+} and the conduction band will vary and this is important in the discussion of luminescent properties such as quenching behaviors and persistent luminescence. Extensive work by Ueda et al. has considered the behavior of excited electrons in the $5d$ levels of garnets in which the $5d$ levels are close to the conduction band, shown schematically in Fig. 8b.[86] They have combined the energy levels of Ce^{3+}, the positions of VB and CB, and the configuration coordinate diagram of Ce^{3+} in order to understand the luminescence processes of Ce^{3+} in garnet phosphors, especially the quenching process. There are three possible quenching processes: (1) thermal relaxation from the $5d$ potential curve (parabola) to the $4f$ ground potential curve through the crossing point based on the configurational coordinate model, (2) thermal ionization from the emitting $5d_1$ levels to the conduction band with some activation energy (thermally assisted photoionization of the Ce^{3+} ion) and (3) direct electron transfer from (higher) $5d$ levels to the conduction band with no activation energy (photoionization of the Ce^{3+} ion) prior to relaxation to the lowest $5d_1$ state. The electrons transferred to the conduction band can be (4) captured by electron traps and then (5) released from the traps through a thermally activated process which is the mechanism behind afterglow or thermally stimulated luminescence. In addition, energy transfer to defects or impurities, possibly via energy migration over multiple Ce^{3+} ions, can also contribute to quenching. These quenching processes are not intrinsic to the material and could be avoided by optimizing synthesis conditions. It is important to distinguish between intrinsic quenching, a material property related to the energy level structure of the Ce^{3+} ion and the host lattice, and extrinsic quenching processes related to the presence of energy transfer and migration to defects and impurities which occur especially at high Ce^{3+} concentrations and strongly depend on the synthesis procedure.

The optical properties of Ce^{3+} in different garnet compounds vary. Although the basic luminescence theory and luminescence mechanism are known, questions remain, such as: How can the compositional substitution and the corresponding modification influence the Ce^{3+} luminescence in different garnet compounds? How can we find new and efficient Ce^{3+}-doped garnet phosphors? What determines the luminescence quenching at elevated temperatures and how can we reduce quenching processes? There are still many challenges in this field. We will summarize important results reported for Ce^{3+} luminescence in a variety of garnet phosphors and propose models to explain the luminescence behavior in relation to structure in the following section. The amount of research in the field is still expanding and it is not possible to review all findings.

2. $Ln_3(M^{IV},M^{VI})_5O_{12}$-based Garnet Phosphor and their Structural Modification

2.1 Structural modification on Ln sites for LnAG:Ce^{3+} (Ln=Y, Lu, Gd and Tb) phosphors

In this section we will review the influence of substituting the trivalent ion on the largest cation site in the garnet host: the dodecahedral site. Trivalent cerium ions doped rare earth aluminum garnets with the general formula $Ln_3Al_5O_{12}$:Ce^{3+} (Ln =

Y, Lu, Gd and Tb) (LnAG:Ce^{3+}) form a very important class of functional optical materials. They have found numerous different applications over the years.[1-5] Presently, LnAG:Ce^{3+} phosphors are intensively studied for their application as LED-phosphor, and Ce^{3+}-doped $Y_3Al_5O_{12}$ is the most famous and first commercially applied phosphor in *w*-LEDs owing to its excellent optical, physical and chemical properties. As mentioned above, YAG:Ce^{3+} can be used to convert part of the blue emission from an (In,Ga)N LED into yellow emission and together the transmitted blue light this produces white light. In many white light LEDs, including those in mobile phone lights, the yellow powder can be clearly recognized by looking in the LED (when turned off).

YAG:Ce^{3+} combines good chemical and thermal stability with a high luminescence efficiency, although the thermal quenching of luminescence remains an issue. Blasse et al. made systematic spectroscopic investigations on YAG:Ce^{3+} in 1967.[1] Owing to the strong crystal field splitting of the 5*d* energy level of Ce^{3+}, excitation of YAG:Ce^{3+} from the $^2F_{5/2}$ level to the lowest-energy 5d orbital ($5d_1$) occurs in a broad spectral range in the blue spectral region with a maximum at ~460 nm, and emission occurs at ~540 nm from the transition of Ce^{3+} from the $5d_1$ orbital to the two 4*f* levels split by spin-orbit coupling into $^2F_{5/2}$ and $^2F_{7/2}$. Fig. 9 gives the photoluminescence excitation, emission spectra and diffuse reflectance spectra of YAG:Ce^{3+} phosphors with different Ce^{3+} concentrations. The two main excitation bands at 340 and 460 nm are ascribed to the electronic transitions from the ground state ($^2F_{5/2}$) to different energy levels of the 5*d* excited state of Ce^{3+} ($5d_2$ and $5d_1$, respectively), as also demonstrated by the diffuse reflectance spectra in Fig. 9(b). Although the 5*d* orbitals of Ce^{3+} can be split into a maximum of five energy levels, only the lowest two have been assigned with certainty. A third weak band in the 250-280 nm range has been assigned both to the Ce^{3+} $5d_3$ absorption and to the impurity/defect absorptions. Later work by Tanner indicated that this is a defect related band. Higher energy bands between 200 and 230 nm have been identified in several publications as higher energy t_{2g} related bands. The tentative positions of the five 5*d* bands for YAG:Ce^{3+} are around 460, 340, 225, and 205 nm, respectively.[90] The fifth band is between 225 and 205 nm, probably close to the 225 nm band and weak. The intense absorption peak around 460 nm matches very well the blue emission of InGaN-based LEDs, indicating that the YAG:Ce^{3+} phosphor can absorb the blue light efficiently and convert it into visible light at a longer-wavelength range. The emission spectrum of YAG:Ce^{3+} shows a very broad yellow band with the emission peak at near 532 nm for the lowest Ce^{3+} concentrations and a full width at half maximum (FWHM) of ~120 nm, which can be assigned to the $5d_1 \rightarrow 4f$ electronic transitions.

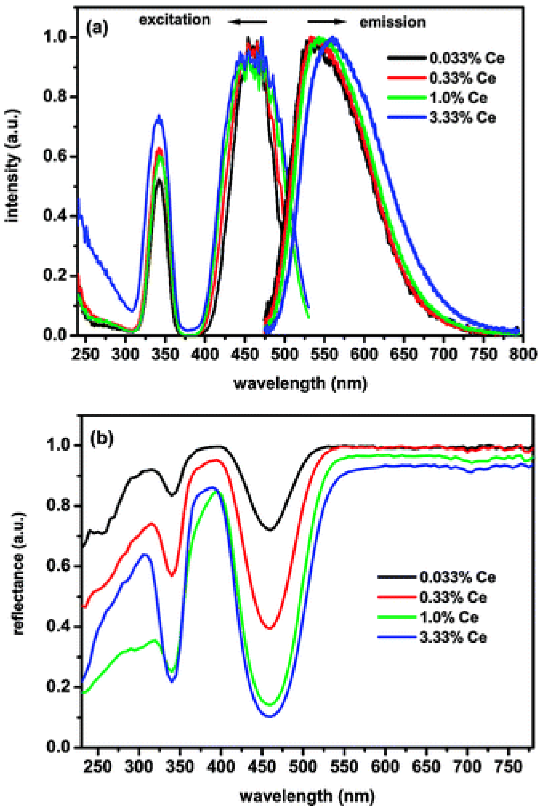

Fig. 9 (a) Photoluminescence excitation (PLE) and emission (PL) spectra of YAG:*x*%Ce^{3+} (concentration in mole% relative to Y^{3+}) for different Ce^{3+} concentrations (*x*), (b) Diffuse reflectance spectra of the same YAG:Ce^{3+} samples. (Reproduced with permission from ref. 15, copyright 2009, American Chemical Society)

For application of YAG:Ce^{3+} in *w*-LEDs the combination of blue and yellow results in cool white light and spectral shifting of the Ce^{3+} emission to the red spectral region is desired to create a warmer white, as discussed above. A simple way of red shifting the emission is increasing the Ce^{3+} concentration. In Fig. 9(a) it can be observed that the emission maximum of the $5d_1 \rightarrow 4f$ emission of Ce^{3+} shifts from ~530 nm for 0.033% Ce^{3+} to ~560 nm for 3.33% Ce^{3+}. Two effects contribute to the spectral shift: reabsorption at the short wavelength Ce^{3+} emission and energy migration to slightly distorted Ce^{3+} ions. The red shift because of reabsorption occurs as there is an overlap between the short wavelength side of the Ce^{3+} emission and the long wavelength tail of the Ce^{3+} absorption. In Fig. 9 the spectral overlap in the 480-530 nm can be clearly observed. As a result, with increasing Ce^{3+} concentration the probability for absorption of the short wavelength side of the Ce^{3+} emission band increases. After reabsorption, emission is distributed over the full width of the Ce^{3+} emission band resulting in an overall decrease of the short wavelength emission and a red shifted emission. The higher the number of reabsorption events, the larger the red shift. The second effect is caused by energy transfer between neighboring Ce^{3+} ions. For high Ce^{3+} concentrations this leads to energy migration of the excitation energy and distorted Ce^{3+} ions, located close to a defect, can experience a larger crystal field splitting, shifting the lowest 5*d* state to a lower energy. Excitation energy is trapped at these distorted sites as a result of energy migration and this effect also contributes to a red shift of the Ce^{3+} emission at elevated Ce^{3+} concentrations. The energy migration increases with temperature as the spectral overlap increases as a result of thermal broadening of the excitation and emission band. Thermally activated energy migration to quenching sites is responsible for a lower thermal quenching temperature for highly doped YAG:Ce^{3+} phosphors as will be discussed below.

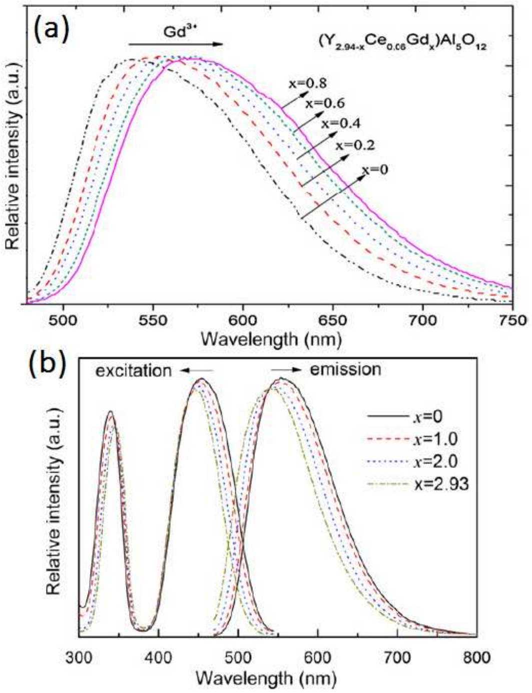

Fig. 10 (a) Emission spectra (λ_{ex} = 460 nm) of $Y_{2.94-x}Gd_xAl_5O_{12}:Ce_{0.06}$ phosphors for different Gd content (x values). (b) Emission and excitation spectra of $Y_{2.93-x}Lu_xAl_5O_{12}:Ce_{0.07}$ phosphors for increasing Lu-content (x values). (Reprinted with permission from ref. 91 and ref. 92, copyright 2011 and 2012, Elsevier.)

A second approach to shift the Ce^{3+} emission is through cation substitution. Empirically it was observed that the emission band of Ce^{3+} in garnets shifted towards the blue when the dodecahedral site (Y^{3+}) ions were substituted by smaller Lu^{3+} ions, and towards the red when Y^{3+} ions were replaced by larger ions such as La^{3+}, Gd^{3+} and Tb^{3+}.[91-93] Therefore, Ce-activated aluminum garnet phosphors can be prepared with Gd, Tb or Lu instead of Y in order to obtain the color-tunable garnet phosphors with emission colors varying from the green to the orange. This approach to alter the emission color. For example a red shift is found for $Gd_3Al_5O_{12}$:Ce^{3+} (GAG:Ce^{3+}) compared with YAG:Ce^{3+}, and has been applied to shift spectrum of white LEDs to obtain a warmer white. Unfortunately, the red shifted emission of Ce^{3+} in these garnet compounds has worse thermal quenching behavior and a lower quantum efficiency compared with YAG:Ce^{3+}. The origin of the lower thermal quenching temperature for Ce^{3+} in GAG will be discussed below. Consequently, GAG is not as widely applied as a host as YAG, also because it is very difficult to synthesize by conventional methods.[94, 95] The substitution of ions in the dodecahedral site induces lattice expansion or contraction and changes the local crystal field interaction of Ce. An example is presented in Fig. 10(a), clearly showing the red shift of the Ce^{3+} emission band with the substitution of Gd^{3+} for Y^{3+}. It can be seen that the emission peak wavelength of $(Y_{2.94-x}Ce_{0.06}Gd_x)Al_5O_{12}$ shifted from 532 nm to 568 nm upon raising the Gd^{3+} concentration. Because the ionic radius of Gd^{3+} (0.105 nm) is larger than that of Y^{3+} (0.102 nm) in a dodecahedral coordination, one could expect the substitution of Gd ion to cause a Ce–O lengthening because of the larger size of the cation site for Ce^{3+} in the garnet host with Gd^{3+}. The red shift of the emission and increase in the energy separation between the $5d_1$ and $5d_2$ level shows an increase in crystal field splitting. This increase in crystal field splitting can be explained by a larger tetragonal distortion of the cuboctahedron around the Ce^{3+} ion. The larger distortion increases the $5d_1$ – $5d_2$ splitting and shifts the lowest energy level of Ce $5d$ state down and consequently induces a red shift of the Ce^{3+} emission. Chiang et al. have also reported that Gd^{3+} substituting Tb^{3+} in $Tb_3Al_5O_{12}$:Ce^{3+} phosphors can induce a red shift and at the same time lowers the thermal quenching temperature.[95]

Next to the yellow-emitting YAG:Ce^{3}+, the Lu analogue LuAG:Ce^{3+} is another important commercial LED phosphors with green emission. However, it has been investigated to a lesser extent.[81] In fact, LuAG:Ce^{3+} has been mainly reported for use as a scintillator.[46, 47, 96, 97] Compared to lower density YAG host lattice (ρ_{YAG} = 4.56 g/cm^3), LuAG has a high density (ρ_{LuAG} = 6.73 g/cm^3) and high effective atomic number (Z_{eff} = 60) and therefore high stopping power for ionizing radiation. Thus, LuAG:Ce^{3+} is regarded as a particularly promising scintillator due to its allowed electric dipole $5d$–$4f$ transition (short emission life time) and high theoretical light yield.[98, 99] The PLE spectra of a typical LuAG:Ce^{3+} phosphor contains two bands: a weak band with the maximum peak at near 345 nm ($5d_2$) and a strong broad band in the spectral range from 400 to 490 nm with the maximum peak at near 455 nm ($5d_1$). The PL spectra show broad emission spectra (spectral range between 480 and 600 nm), with the maximum peak intensity at 507 nm.[100] Fig. 10(b) presents the typical excitation and emission spectra of $Y_{2.93-x}Lu_xAl_5O_{12}:Ce_{0.07}$ phosphors with various x values (x = 0, 1.0, 2.0 and 2.93). The lattice parameters of $Y_{2.93-x}Lu_xAl_5O_{12}:Ce_{0.07}$ slightly decrease with increasing Lu^{3+} content, due to the smaller ion radius of Lu^{3+} (0.098 nm) compared with Y^{3+} (0.102 nm). As seen in Fig. 10(b), the emission and excitation maxima shift linearly to shorter wavelengths with increasing Lu^{3+} content for the $5d_1$ level, while the $5d_2$ level shifts to slightly longer wavelengths, indicating that the $5d_1$-$5d_2$ crystal field splitting decreases upon substitution of Y^{3+} by Lu^{3+}. As discussed, these emission shifts have been correlated to the tetragonal distortion around Ce^{3+} ions by chemical substitution in garnet hosts.[91]

$Tb_3Al_5O_{12}$ (TAG) garnet doped with Ce^{3+} is a suitable optical material for w-LEDs and scintillators. Compared with LuAG:Ce^{3+} and YAG:Ce^{3+}, the Ce^{3+} emission spectrum in TAG:Ce is significantly shifted to the red. In TAG:Ce^{3+} garnet, the presence of an effective energy transfer from the matrix (Tb^{3+} cations) to the Ce^{3+} activator has been studied in detail.[101-104] The $^5D_4$ level of Tb and $5d_1$ level of Ce^{3+} are very close in energy and at room temperature energy transfer occurs in both directions (from Ce to Tb and back). The dynamics of energy transfer between Ce^{3+} and Tb^{3+} have been studied by analysis of time dependent luminescence decay curves.[99, 105] The long lived $^5D_4$ level of Tb^{3+} can act as a reservoir for the excitation energy and give rise to slower decay dynamics of the emission, which is undesired in applications where a short decay is required (e.g. in scintillators for PET-scanners). Ce^{3+}-activated TAG was also a novel phosphor for warm white LED application as reported by Kummer.[28] In Fig. 11 the typical excitation and emission spectra of TAG:Ce^{3+} are shown. The excitation spectrum of the TAG:Ce^{3+} contains $4f^8$–$4f^7 5d$ transition bands at around 276 nm (spin-allowed, $\Delta S = 0$) and 325 nm (spin-forbidden, $\Delta S = 1$), as well as the f–f transition lines of Tb^{3+} at longer wavelength (377 nm for $^7F_6$–$^5D_3$, etc.). The lowest-energy $5d_1$ excitation band of Ce^{3+} is at about 463 nm. The higher energy $5d_2$ band of Ce^{3+}

overlaps with the spin-forbidden Tb^{3+} 4*f*–5*d* transition. Excitation in the characteristic *f*-*d* absorption band of Tb^{3+} at 276 nm gives rise to the Ce^{3+} $5d_1$ luminescence around 530–550 nm which confirms energy transfer from Tb^{3+} to Ce^{3+}. This can be favorable to enhance the Ce^{3+} emission. Strong and broad green–yellow emission is also found under 463 nm light excitation (Fig. 11).[29] Recently, Ren et al. reported the crystal growth, structure, optical and scintillation properties of Ce^{3+}-doped $Tb_{2.2}Lu_{0.8}Al_5O_{12}$ single crystals, and found that Ce^{3+}-doped crystals showed not only *f*-d absorption bands, but also the typical 4*f*–4*f* absorption of Tb^{3+}. Under x-ray and UV excitation, strong emission peaks at 530 nm and 565 nm and the line emission traces of 4*f*–4*f* transitions featuring Tb^{3+} were both observed for the Ce^{3+}-doped crystal.[48]

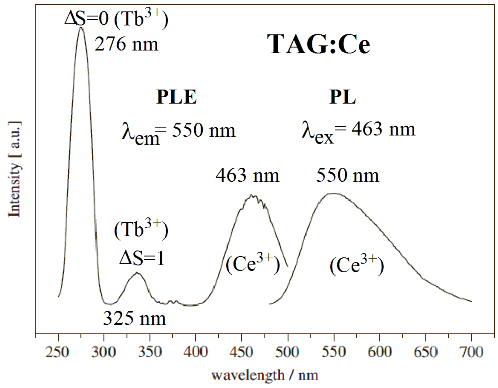

Fig. 11 PLE and PL spectra of $Tb_{2.97}Al_5O_{12}:0.03Ce^{3+}$. (Reprinted with permission from ref. 102, copyright 2007, Elsevier.)

In summary, the excitation and emission spectra of Ce^{3+} are similar in the LnAG:Ce^{3+} (Ln=Y, Lu, Gd and Tb) garnet series. When the dodecahedral Ln sites are occupied by a host cation with a smaller ionic radius, such as Lu^{3+}, the crystal field splitting is reduced, shifting the lowest energy Ce^{3+} 5*d* level to higher energy while for substitution of Y^{3+} by the larger Gd^{3+} and Tb^{3+} ions a stronger crystal field shifts the $5d_1$ level of Ce^{3+} to lower energies. A schematic energy diagram for Ce^{3+} in garnet phosphors including YAG, TAG, and GAG is presented in Fig. 12.[94, 106, 107] Note that in this picture also the total crystal field splitting (position of the high energy t_{2g} crystal field components) is drawn as increasing from YAG to TAG to GAG. However, it is not clear and also not expected that this is the case. Also the CB and VB are sketched as bands that do not change in energy between YAG, TAG and GAG. A more realistic band diagram will be presented below in Fig. 25. The change in the $5d_1$-$5d_2$ splitting is well documented and is explained by an increase in the tetragonal distortion of the lower e_g state. As discussed above, the positions of the higher energy $5d_3$, $5d_4$ and $5d_5$ crystal field components are hard to determine experimentally and even for YAG:Ce there is no consensus on the position of the 5*d* bands. Further research is needed to establish the total 5*d* crystal field splitting for Ce^{3+} in TAG and GAG. Based on classic models for the crystal field splitting and opposite behavior to what is observed for the $5d_1$-$5d_2$ splitting would be expected. For Ce^{3+} on the larger Gd or Tb site, the increase in Ce-O ligand distance is expected to result in a smaller overall crystal field splitting.

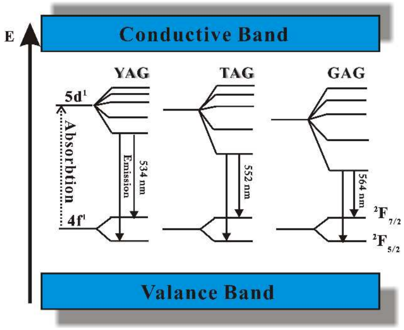

Fig. 12 Schematic energy diagram for Ce^{3+} in YAG, TAG, and GAG and the emission process in Ce^{3+}. Note that in this schematic picture the variation of bandgap with composition is not taken into account. (Reprinted with permission from ref. 94, copyright 2007, The Electrochemistry Society.)

The luminescence temperature-quenching behavior of Ce-doped garnet-type phosphors is very important for practical applications. Especially in *w*-LEDs where phosphors applied directly on the blue emitting (InGa)N chips reach temperatures well above 100 °C, even close to 200 °C in the highest power LEDs. Meijerink et. al. systematically studied the temperature dependence of the emission intensity for YAG with different Ce concentrations, as shown in Fig. 13(a).[15] For low dopant concentrations (0.033%, mole% relative to Y^{3+} in line with the usual notation in luminescent materials where the dopant concentration is in mole% relative to the ion for which the dopant substitutes), the temperature induced variation of the emission intensity varies for different excitation wavelengths within the 460 nm band, while for the higher Ce^{3+} concentrations (3.33%) the quenching temperature is lower and the same for all excitation wavelengths. Furthermore, as an alternative method to probe luminescence quenching, emission lifetime measurement of Ce^{3+} were performed as a function of temperature with various Ce^{3+} contents, shown in Fig 13(b). For higher Ce^{3+} concentrations the luminescence lifetime is slightly longer at room temperature. The emission lifetimes for the samples with high Ce^{3+} content show a strong decrease upon raising the temperature above ~100 °C while for low concentrations a much higher quenching temperature was observed. The difference was explained by thermally activated concentration quenching in samples with higher Ce-concentrations. Based on the analysis it was concluded that the actual quenching temperature for the Ce^{3+} emission in YAG is reflected in the temperature dependent decay times for YAG with low Ce^{3+} concentrations and is very high (>600 K). For practical application in high power LEDs this implies that low Ce-concentrations (<1%) need to be used to prevent temperature quenching.

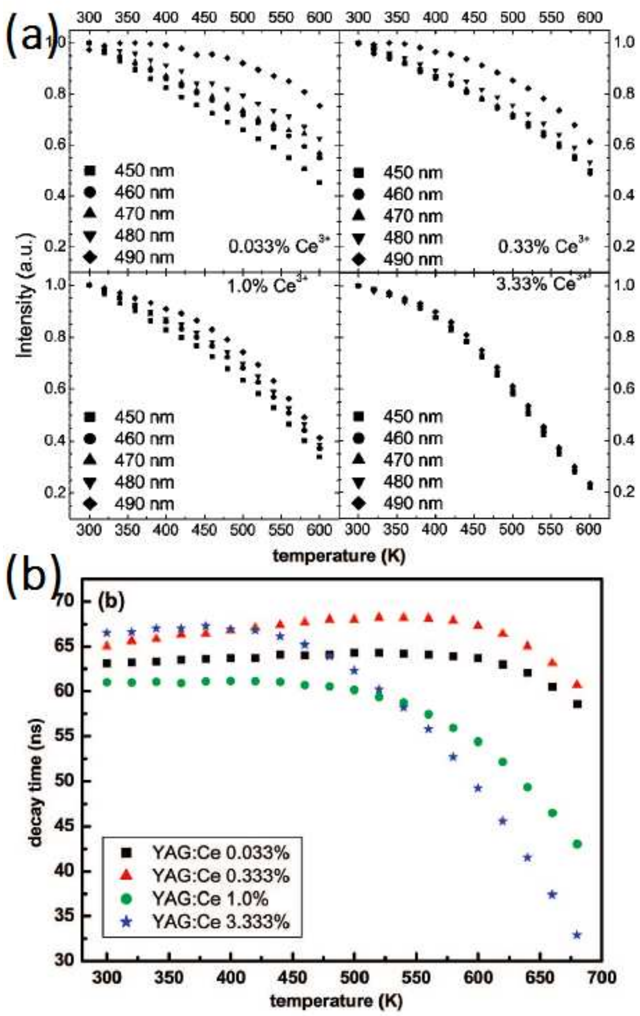

Fig. 13 (a) Temperature dependence of the emission intensity for YAG with different Ce concentration for different excitation wavelengths (indicated in figure). (b) Decay times of YAG:Ce determined from single-exponential fits of the luminescence decay. (Reprinted with permission from ref. 15, copyright 2009, American Chemical Society.)

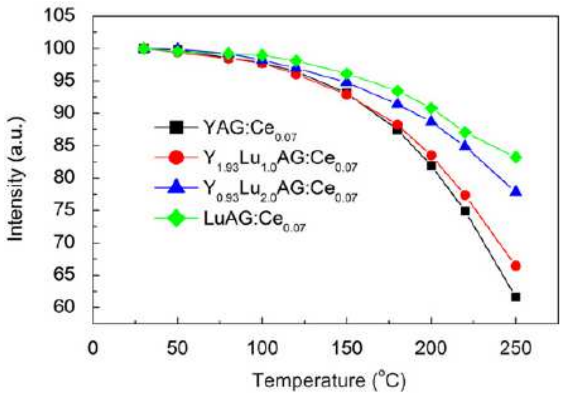

Fig. 14 Temperature dependences of the integrated emission intensity of $Y_{2.93-x}Lu_xAl_5O_{12}:Ce_{0.07}$ phosphors excited by 460nm light. (Reprinted with permission from ref. 91, copyright 2011, Elsevier.)

Significant changes in temperature-dependent characteristic of Ce^{3+} emission can be observed as Y^{3+} ions are replaced by Gd^{3+} or Lu^{3+} ions. The incorporation of Gd^{3+} will lower the quenching temperature of YAG:Ce^{3+} emission while the introduction of Lu^{3+} has been reported to have the opposite effect.[108] An example is presented in Fig. 14, showing the variations of the emission intensity for $Y_{2.93-x}Lu_xAl_5O_{12}:Ce_{0.07}$ phosphors ($x = 0, 1.0, 2.0, 2.93$) with increasing temperature.[91] It can be found that with increasing Lu^{3+} substitution the thermal quenching temperature of the Ce^{3+} emission can be improved. It is important to note that the high Ce-concentrations used in these Lu substitution experiments give rise to thermally activated concentration quenching. The influence on the quenching temperature of the intrinsic Ce^{3+} emission in LuAG vs. YAG is not known. To investigate the influence of Y-Lu substitution on the intrinsic quenching temperature of the isolated Ce^{3+} centers, the thermal quenching of the Ce^{3+} in LuAG with low Ce^{3+} concentrations are required. Indeed, experiments on low doped (0.3%) LuAG:Ce^{3+} revealed an even higher intrinsic Ce^{3+} luminescence quenching temperature (>700 K) in comparison to YAG:Ce^{3+}.[109]

The results presented above reveal that the quenching temperature of the Ce^{3+} emission can be very high and well above the temperatures reached for on-chip phosphors even in high power LEDs which can be 150-200 °C. However, the quenching temperature strongly varies between garnets with different cations on the dodecahedral position. To explain the variation in the quenching temperature, initially it has been suggested that thermally activated cross-over from the 5*d* excited state to the 4*f* ground is responsible.[95] The redshift of the emission on going from YAG to TAG to GAG can explain a decrease in the activation barrier for cross-over as shown in Fig. 15. However, later experiments by Ueda et al. demonstrated that thermally activated photoionization is the mechanism responsible for the lowering of the quenching temperature upon substitution of Y by Tb or Gd.[110, 111] Herein, YAGG denotes the $Y_3(Al,Ga)_5O_{12}$ phosphor, which will be discussed in the following section. The quenching temperature is lowest for Ce^{3+} in GAG where the energy difference between the $5d_1$ state and the conduction band edge is smallest. The activation energy for ionization from the $5d_1$ state to the conduction band decreases in the order of $\Delta E_{YAG} > \Delta E_{TAG} > \Delta E_{GAG}$.

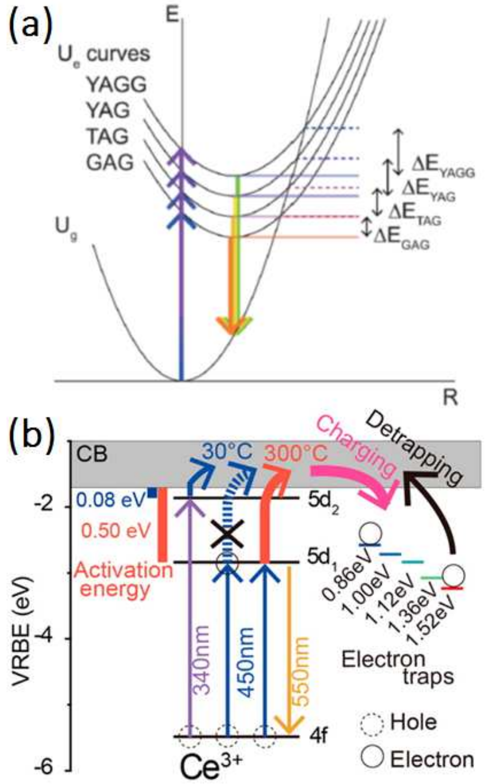

Fig. 15 (a) Configuration coordinate diagram of Ce^{3+} in YAGG, YAG, TAG, and GAG host initially suggested to explain the variation in quenching temperature. (Reprinted with permission from ref. 110, copyright 2011, AIP Publishing LLC.) and (b) Thermally activated photoionization mechanism responsible for the quenching of the Ce^{3+} emission in YAG as determined by thermoluminescence excitation spectroscopy (Reprinted with permission from ref. 111, copyright 2015, American Chemical Society.)

2.2 Structural modification on M/M' sites for $Ln_3(M,M')_5O_{12}$:Ce^{3+} phosphors

In the crystal structure of garnet-type $Y_3Al_5O_{12}$, Al^{3+} ions occupy two different sites: two of the five aluminum cations occupy octahedral sites (six-coordinated [AlO_6]) and three occupy tetrahedral sites (four-coordinated [AlO_4]). This provides a second and even more versatile strategy of structural modification to tune the luminescence properties of Ce^{3+}. Cation substitutions on the tetrahedral and octahedral M/M' sites for garnet-type $Ln_3(M,M')_5O_{12}$ allow for different substitutions on both M and M' sites: M=Al, Ga, Si, Ge…; M'=Al, Ga, Sc, Sb... Substitutions on these sites influence the stability of the garnet phases, the band structure and affect the luminescence properties of dopants as Ce^{3+}. The parameter space is even wider than that for substitution of the Ln site. For example, Al^{3+} can be replaced by the larger Ga^{3+} or the even larger Sc^{3+}. More complex aliovalent substitutions are also possible: Two Al^{3+} ions can be replaced by one Mg^{2+} plus one Si^{4+} or Ge^{4+} while maintaining charge neutrality and the garnet crystal structure. Many other substitutions are also possible.[34-36] Herein, we will discuss how to form stable garnet phases and the effect on the luminescence of Ce^{3+} will be reviewed and discussed.

The color point of the YAG:Ce phosphor can be tailored by varying the crystal field through cation substitutions in the host lattice with the general rule that an increased diameter of the ion on the dodecahedral site results in an increased crystal field splitting for the $5d_1$ and $5d_2$ level, shifting the emitting $5d_1$ state to lower energies (see section 2.1). An increased diameter of the ion substituting on the octahedral site results in a decreased crystal field splitting. Ga^{3+} ion is one of the ions which substitute at both the tetrahedral and octahedral sites in the garnet lattice. Partial replacement of Al with Ga leads to a blue-shift of both the lowest energy Ce^{3+} $4f^1 \rightarrow 5d^1$ excitation and $5d^1 \rightarrow 4f^1$ emission band. Yadav et. al. reported the $Y_3Al_3Ga_2O_{12}$:Ce^{3+} and $Y_3Al_4GaO_{12}$:Ce^{3+} phosphors. For $Y_3Al_4GaO_{12}$:Ce^{3+} the emission band is around 519 nm and the $5d_1$ excitation band is at 450 nm. The emission spectrum of $Y_3Al_3Ga_2O_{12}$:Ce^{3+} shows a 511 nm Ce^{3+} *d-f* emission, which is a significant blue shift compared to the 532 nm of YAG:Ce.[30]

The optical properties of $Gd_3(Al,Ga)_5O_{12}$:Ce^{3+} scintillators were also investigated as a function of the Ga/Al ratio by Ogiegło et. al.[99] The two lowest energy excitation bands of Ce^{3+} are located between 400~540 nm and 320~370 nm, corresponding to $5d_1$ and $5d_2$ bands, respectively. When the Ga^{3+} content is increased, the crystal field splitting decreases. As a result, the higher $5d_2$ excitation band shifts toward lower energy and, at the same time, the lowest $5d_1$ excitation and emission bands move toward higher energies. Furthermore, if Ga^{3+} is substituted only in octahedral sites, the band gap was not affected, however, as soon as octahedral sites were fully occupied by Ga^{3+} and the ions started substituting in tetrahedral sites, the band gap was observed to decrease in energy reflecting the tetrahedral aluminate groups being involved in the lower energy orbitals of the conduction band. It was also observed that $Gd_3Ga_2Al_3O_{12}$:Ce^{3+} with all octahedral sites occupied shows the highest emission intensity with great potential as scintillator materials in the fields of medical imaging and high energy and nuclear physics detectors.[112-114]

In Fig. 16, the excitation spectra at room temperature (RT) of Ce^{3+}-doped $Gd_3(Ga,Al)_5O_{12}$ samples are shown. For the pure gallate $Gd_3Ga_5O_{12}$:Ce1%, strong quenching occurs and no emission is observed, not even at cryogenic temperatures.[50] The spectra in Fig. 16 exhibit two excitation bands of Ce^{3+}, a $5d_1$ band between 400 and 540 nm, and a $5d_2$ band between 320 and 370 nm. To investigate the shift of the *5d* band maxima, normalized spectra are shown in the insets (a) and (b). With increasing amount of Ga^{3+} the higher energy $5d_2$ band red shifts toward longer wavelength, whereas a blue shift is recorded for the lowest $5d_1$ absorption band (inset b). Fig.16(a) depicts the emission spectra of $Gd_3(Ga,Al)_5O_{12}$:Ce1% samples measured for excitation at 445 nm at RT. The inset shows the normalized spectra which allows for quantification of the shift in the *5d* band positions. It is observed that the emission maxima for the samples with increasing Ga^{3+} content shift to shorter wavelengths, similar as observed in Ga substituted YAG:Ce^{3+}.[50]

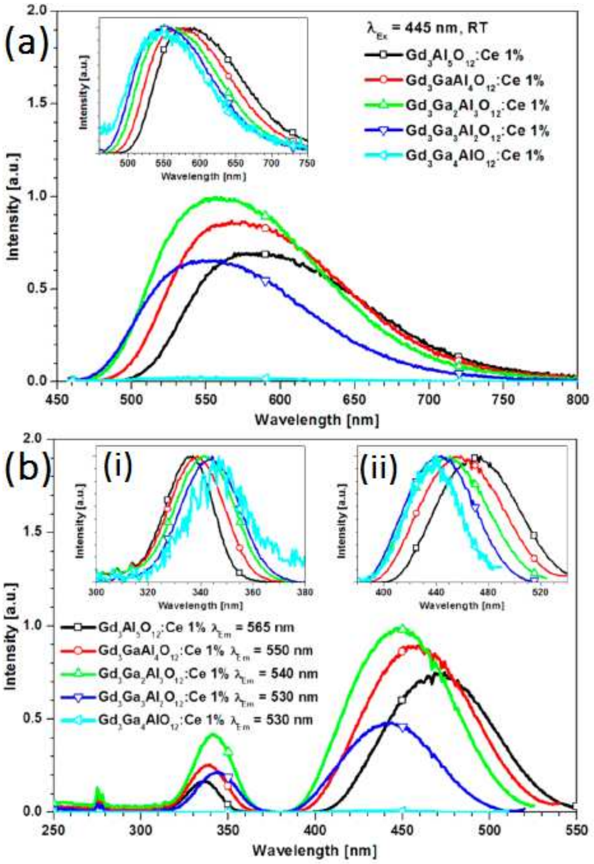

Fig. 16 (a) Emission spectra for $Gd_3(Ga,Al)_5O_{12}$:Ce1% measured for excitation at 445 nm at room temperature. The inset shows the normalized emission spectra. (b) Room temperature excitation spectra measured at the emission maxima of the Ce^{3+} emission. The shifts are clearly visible in insets (i) and (ii), which show the normalized excitation bands of the two lowest 5*d* states. (Reprinted with permission from ref. 50, copyright 2013, American Chemical Society.)

Ueda et. al. did systematic research on Sc-doped garnet-type $Y_3Sc_2Al_{3-x}Ga_xO_{12}$:$Ce^{3+}$ phosphors.[51, 86, 110] Among them, $Y_3Sc_2Ga_3O_{12}$:Ce^{3+} (YSGG:Ce^{3+}) shows a beautiful green long-lasting afterglow after blue excitation, not requiring UV excitation for efficient afterglow. This is a great advantage over the classical afterglow material $SrAl_2O_4$:Eu^{2+}, Dy^{3+} that is most efficiently charged with UV-radiation. Afterglow luminescence of Ce^{3+}-doped garnets is a rapidly expanding field and also here cation substitution offers the possibility to tune and optimize the afterglow characteristics. Already in 1969 Holloway and Kestigian mentioned observation of the afterglow luminescence in $Y_3Al_2Ga_3O_{12}$:Ce^{3+} and $Y_3Al_{1.5}Ga_{3.5}O_{12}$:$Ce^{3+}$ by UV excitation.[54] Later, Kanai et al. reported the afterglow properties of $Gd_{3+\delta}(Al,Ga)_{5-\delta}O_{12}$:$Ce^{3+}$ in the time range of ms after X-ray excitation [115] Fig. 17 shows photographs of the as-made and O_2-annealed YSGG:Ce^{3+} ceramics under ambient light, under UV excitation and after excitation. The green luminescence and afterglow luminescence were observed in both YSGG:Ce^{3+} ceramics by during UV excitation and after excitation.[51] The afterglow intensity is observed to be less intense for the material annealed in oxygen, which suggests a role of oxygen vacancies in the electron trapping process. Just as for the well-known afterglow material $SrAl_2O_4$:Eu^{2+}, Dy^{3+} it is not easy to identify the nature of the traps involved in electron trapping [116]

A series of solid solution of Ce^{3+}-doped $Y_3Sc_2(Al,Ga)_3O_{12}$ phosphors were discussed recently by Ueda et al.[85, 86] The Sc ion will substitute on the octahedral sites. Subsequently part of the tetrahedral Al^{3+} was replaced by Ga^{3+}. The PL spectra excited at 440 nm and the PLE spectra of the Ce luminescence from the samples are shown in Fig. 18a. The luminescence peak in the $Y_3Sc_2Al_3O_{12}$:Ce (YSAG:Ce), $Y_3Sc_2Al_2GaO_{12}$ (YSA2G1G:Ce), $Y_3Sc_2AlGa_2O_{12}$ (YSA1G2G:Ce) and $Y_3Sc_2Ga_3O_{12}$ (YSGG:Ce) are located at 520, 510, 500 and 496 nm, respectively. The luminescence peak blue-shifts with increasing Ga content. In the PLE spectra, the two excitation bands observed at approximately 340 nm and 430 nm are attributed to transitions from the 4*f* ground level to the $5d_1$ and $5d_2$ levels. The transition energies of Ce^{3+} in the samples are shown as a function of the lattice constant in Fig. 18b. The $4f$–$5d_2$ excitation band shifts to lower energies and the $4f$–$5d_1$ excitation and emission peaks shift to higher energies with increasing lattice constant. The blue shift of the $5d_1$ level with increasing Ga content at the tetrahedral site is caused mainly by a decrease in $5d_1$-$5d_2$ crystal field splitting (Δ_{12}) not by a centroid-shift.[117]

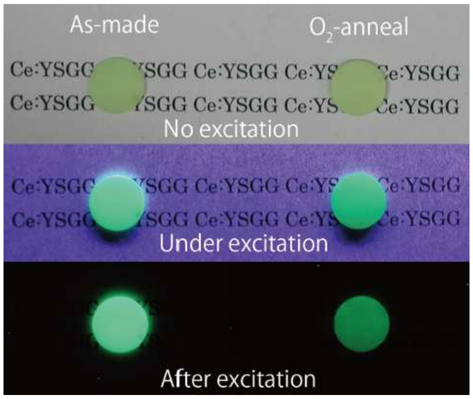

Fig. 17 Images of the as-made and O_2-annealed YSGG:Ce^{3+} ceramics in ambient light, under UV excitation, and in the dark after UV excitation. (Reprinted with permission from ref. 51, copyright 2011, IOP Publishing.)

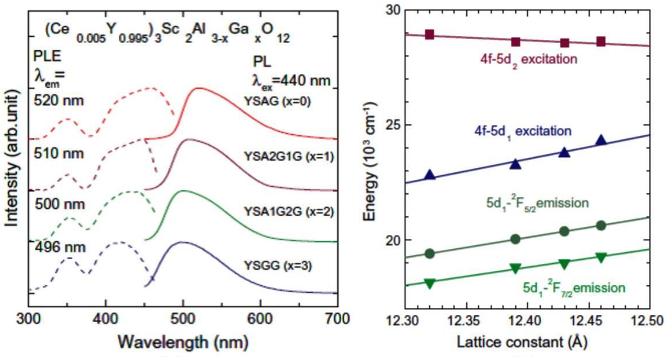

Fig. 18 (a) PL and PLE spectra of the YSAGG:Ce^{3+} solid solutions; (b) Lattice constant dependence of transitions energies of the Ce^{3+} excitation bands in YSAGG:Ce^{3+} solid solutions. (Reprinted with permission from ref. 86, copyright 2013, Elsevier.)

Substitution of Sb^{3+} has been studied in a variety of LnAG (Ln = Y, Tb, Gd) hosts. Sb^{3+} will substitute on the octahedral sites in garnet phosphors.[31] Fig. 19 shows the emission spectra of Ce^{3+}-doped $Y_3(SbAl)Al_3O_{12}$, $Tb_3(SbAl)Al_3O_{12}$,

$Gd_3(SbAl)A1_3O_{12}$ and $Gd_3(SbGa)A1_3O_{12}$ under 465 nm excitation. Emission peak maxima are at 543, 553, 555 and 554 nm, respectively. The wavelengths for the emission maxima of Ce^{3+}-doped $Tb_3(SbAl)A1_3O_{12}$ and $Gd_3(SbGa)A1_3O_{12}$ were longer than that for Ce^{3+}-doped $Y_3Al_5O_{12}$. It is also found that the substitution of Sb^{3+} ion on an octahedral site causes a blueshift as compared to the Ce^{3+} emission in the pure aluminates. In addition an increase in the width of the emission band is observed in comparison to YAG:Ce^{3+}.[31] The blue shift can be explained by the larger ionic radius of Sb^{3+} compared to Al^{3+} and the effect is similar to that of replacing Al^{3+} by Ga^{3+}. The broadening can result from disorder in the occupation of the octahedral sites by Al^{3+} and Sb^{3+} as only half the octahedral sites are filled by Sb^{3+}. This will result in Ce^{3+} with more or less Sb^{3+} in neighboring O_h sites and this will give rise in a variation of the energy of the $5d_1$ state causing inhomogeneous broadening.

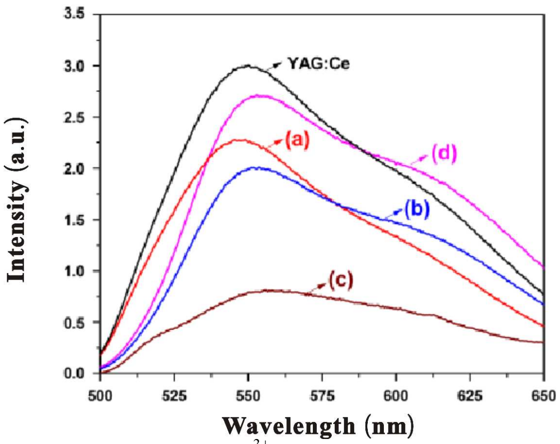

Fig. 19 PL spectra of Ce^{3+}-doped $Y_3(SbAl)A1_3O_{12}$ (a), $Tb_3(SbAl)A1_3O_{12}$ (b), and $Gd_3(SbAl)A1_3O_{12}$ (c), $Gd_3(SbGa)A1_3O_{12}$ (d) and YAG:Ce^{3+} phosphors. (Reprinted with permission from ref. 31, copyright 2011, Wiley.)

In addition to equivalent substitution on the two different sites on M/M' sites by trivalent ions (Al, Ga, Sc or Sb) also substitution of two Al^{3+} ions by a Mg^{2+}–Si^{4+} pair has been explored and was shown to cause a red shift of the Ce^{3+} emission.[118] Such a charge-balanced substitution with aliovalent cations allows for a stable single-phase structure of the doubly-substituted garnet and has been extensively reported by Katelnikovas, Setlur and Maniquiz.[34-38, 119, 120]

The coordination for the dodecahedral site for Ce^{3+} changes as a result of the substitution and it will induce color-tunable luminescence from Ce^{3+} in garnet phosphors. For example, $[AlO_4]^{5-}$ and $[AlO_6]^{9-}$ groups are replaced by $[SiO_4]^{4-}$ and $[MgO_6]^{10-}$, respectively. The octahedron around Mg ions is characterized by an increased alkalinity of O^{2-} anions leading to a more covalent character of the host lattice. Therefore, a double substitution of Mg^{2+}–Si^{4+} for Al^{3+}-Al^{3+} in Al-based garnet results in a red shift of the Ce^{3+} emission band.[121]

As an example on the substitution of Mg^{2+}–Si^{4+} pair, the emission spectra of $Y_3Mg_2AlSi_2O_{12}$:Ce^{3+} (YMASG:Ce^{3+}) are shown in Fig. 20, giving the normalized PL spectra of YMASG:Ce^{3+} phosphors with different Ce content and the PL spectrum of YAG:0.05Ce^{3+} for comparison. The striking feature of the YMASG:Ce^{3+} emission is a remarkably large red shift of the band by ~50 nm compared to that of YAG:Ce^{3+}. It is argued that the red shift of Ce^{3+} emission in YMASG is a combination of increased covalency and Stokes shift. As no excitation spectra are shown in the paper, it is not clear if an increase in crystal field splitting between $5d_1$ and $5d_2$ also contributes to the red shift. Jüstel's group also reported the $Y_{3-x}Lu_xAl_3MgSiO_{12}$:$Ce^{3+}$ phosphors and proposed that the phosphors showing red-shifted emission in comparison with commercial YAG:Ce^{3+} phosphors enable warmer white LED light sources if combined with a blue emitting InGaN chip. However, quite strong concentration and thermal quenching was observed for the red-shifted emission. Luo et. al. also reported the luminescence properties of Mg–Si co-doped $Tb_3Al_5O_{12}$:Ce^{3+} showing a maximum emission intensity in the 554–575 nm range when exciting at 462 nm. The emission peak is redshifted to orange–yellow by increasing the concentration of Mg^{2+}–Si^{4+} pairs. The redshift of the TAG:Ce^{3+} is explained by an increased crystal field splitting and changes of covalent character.[122]

The shift in Ce^{3+} emission wavelength is assigned to either crystal field splitting or covalency (nephelauxetic) effects with sometimes a small contribution of changes in Stokes shift. The basis for explaining a red shift (or blue shift) with either of the effects is often lacking. It is not easy to distinguish between them. Proof for covalency effects requires an accurate determination of the energy for all 5*d* bands so that the barycenter (degeneracy weighted average energy of the 5*d* state) can be determined. A higher degree of covalency will shift the barycenter to lower energies. The effect of crystal field splitting on the 5d emission wavelength contains contributions from the $5d_1$-$5d_2$ splitting as well as the overall e_g-t_{2g} splitting. Again, for a proper analysis the positions of the high energy 5*d* states is required. Since these have not been determined a definite assignment cannot be made. However, based on the observed large changes in the $5d_1$-$5d_2$ splitting there is strong evidence that this splitting is largely responsible for the observed blue and red shifts. Further evidence that covalency effects are not dominant in case of cation substitution are the results for replacement of Al^{3+} by Ga^{3+}. Gallates are more covalent than aluminates and this is also reflected by a decrease in bandgap upon Ga substitution. In spite of the higher covalency for the gallates, a blue shift is observed for the Ce^{3+} emission. The blue shift is consistent with the reduction in $5d_1$-$5d_2$ splitting.

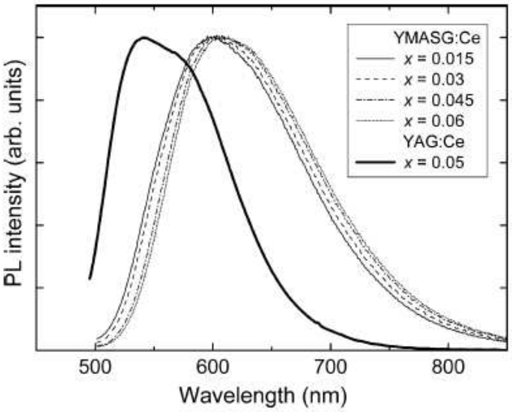

Fig. 20 Normalized PL spectra of YMASG:Ce^{3+} phosphors with different Ce content together with the PL spectrum of YAG:0.05Ce^{3+} for comparison. (Reprinted with permission from ref. 34, copyright 2010, Elsevier.)

The focus on tuning the Ce^{3+} luminecence properties has been on the wide range of options offered by cation substitution. In the literature there are a few paper involving anion substitution and it is worthwhile to briefly mention this here. Both the covalent character and crystal field strength can be increased by partial double replacement of Al–O groups by Si–N, which yields nitride-aluminates.[32, 33, 123] This substitution increases the nephelauxetic effect due to the partial nitrogen coordination of Ce^{3+}, resulting in a red-shift of the emission band. At the same time, also the crystal field splitting is expected to increase. In 2008, Setlur et al. reported that the energy levels of Ce^{3+} were lowered with the incorporation of Si-N into the garnet lattice, which makes nitrido-YAG:Ce promising for creating warm white LEDs (with lower correlated color temperatures (CCTs), <4000 K) and a good color rendering index (CRI), >80).[32] Under 450 nm light excitation, this series of $Y_3Al_{5-x}Si_xO_{12-x}N_x$:Ce ($x$ = 0.2-0.3) all produce strong and broad-band emission peaking around 560 (x = 0), 586 (x = 0.1) and 591 nm (x = 0.2). A similar strategy of incorporating N^{3-} into garnet-type phosphors has also been reported as strategy to modify the emission spectrum of the green phosphor $Ca_3Sc_2Si_3O_{12}:Ce^{3+}$ by enhancing its red emission component and this has been shown to yield an alternative for achieving a single white phosphor. [124, 125]

2.3 Ce^{3+}-doped $(Ln,Me)_3(M,M')_5O_{12}$-based Solid Solution Phosphors

In the sections above it has been discussed how the Ce^{3+} absorption and emission characteristics in garnets can be tuned by varying crystal field strengths and covalent character through cation substitution on the dodecahedral site or on the octahedral/tetrahedral sites. It is known that garnets based on the lanthanide elements from Gd to Lu substituting for the dodecahedral site, and Sc^{3+} (3A group), Al^{3+}, Ga^{3+} (3B group) substituting for octahedral site are stable. An even more complex cation substitution scheme to control the optical properties involves a combined substitution on dodecahedral and octahedral/tetrahedral sites by cations with different valence. Garnet-type $(Ln,Me)_3(M,M')_5O_{12}$-based solid solution phosphors have been proposed where Me is a divalent cation and one of the trivalent M, M' ions is replaced by a tetravalent ion. As an example, $Y_3Al_5O_{12}$ and $Ca_3Sc_2Si_3O_{12}$ (CSS) are isostructural and involve the replacement of $\{Y^{3+}\}$-$[Al^{3+}]$-(Al^{3+}) in $Y_3Al_5O_{12}$ with $\{Ca^{2+}\}$-$[Sc^{3+}]$-(Si^{4+}) in $Ca_3Sc_2Si_3O_{12}$.[26, 27] Fig. 21 demonstrates the relation between the crystal structures of $Y_3Al_5O_{12}$ and $Ca_3Sc_2Si_3O_{12}$. They have the same structural character except for the different polyhedron substitution of $[AlO_6]$ by $[ScO_6]$, $[AlO_4]$ by $[SiO_4]$ and $[YO_8]$ by $[CaO_8]$.

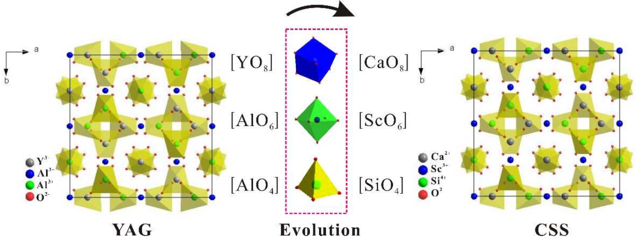

Fig. 21 Evolution of the crystal structures of two garnet phases, YAG (a) and CSS (b) projected from the (001) direction.

Already in 1977, the silicate garnet CSS was reported to crystallize in a cubic crystal system with space group *Ia3d* under ambient pressure.[126] The Ce^{3+}-doped CSS phosphor was proposed by Shimomura in 2007.[26] In this host, the Ce^{3+} ions replace Ca^{2+} on the eight-coordinated dodecahedral site despite the discrepancy of valence between Ce^{3+} and Ca^{2+}. Charge compensation for Ca^{2+} on the Ln^{3+} site is provided by substituting Si^{4+} on an Al^{3+} site. Fig. 22 shows the PL and PLE spectra of the CSS:Ce phosphor. The PL peak wavelength was 505 nm. CSS:Ce^{3+} was also reported to have a higher luminescence quenching temperature for the Ce^{3+} emission than YAG:Ce^{3+}. However, a comparison was made with an (Y,Gd)AG:Ce^{3+} sample with unspecified Ce-concentration, showing quenching starting at temperatures as low as 50 °C. For a proper comparison of quenching temperatures, intrinsic quenching temperatures have to be compared for samples with low doping concentrations.

For the class of garnets with divalent cations on the dodecahedral site, cation substitution has been used to further control and tune the luminescence properties. In this case, the Mg^{2+} substitutes for Sc^{3+} in the 6-coordinated site and provides charge compensation for replacing Ca^{2+} by Ce^{3+}. Therefore, when Mg is introduced into the CSS host, the PL spectra of the CSS:Ce^{3+} phosphors induces a redshift of the Ce-emission with increasing Mg content.[27] The presence of divalent cation sites allows for substituting divalent cations, including luminescent divalent cations. Mn^{2+} may substitute for Ca^{2+} to generate a yellow emission band (574 nm) but can also substitute for Sc^{3+} to generate a red emission band (680 nm). Considerable Mn^{2+} substitution on Sc^{3+} sites can be realized through balancing their charge difference by introducing trivalent rare earth ion, such as La^{3+} and Ce^{3+}, to replace Ca^{2+}. Energy transfer from Ce^{3+} to both Mn^{2+} centers has been observed, resulting in full color luminescence in CSS:Ce^{3+},Mn^{2+}.[127]

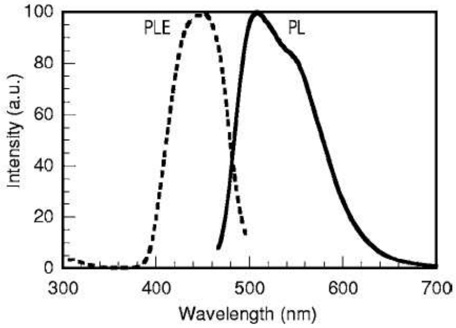

Fig. 22 PL and PLE spectra of $Ca_3Sc_2Si_3O_{12}:Ce^{3+}$. (Reprinted with permission from ref. 26, copyright 2007, The Electrochemistry Society.)

In the garnet $(Ln,Me)_3(M,M')_5O_{12}$ host, a variety of solid solution phosphors exist with Ca^{2+}–Si^{4+} and Mn^{2+}–Si^{4+} substitution for Ln^{3+}-Al^{3+}. Ce^{3+}-doped garnet phosphors of this type have also been reported and received considerable attention in relation to the development of new LED phosphors. Note that this class materials is different from the Mg^{2+}–Si^{4+} substitution for Al^{3+}-Al^{3+} in Al-based garnet phosphors described in Section 2.2.[39, 128-133] The Mg^{2+}–Si^{4+} substitution involved the tetrahedral and octahedral sites, where the Ca^{2+}–Si^{4+} and Mn^{2+}–Si^{4+} substitution involves dodecahedral and tetrahedral sites in the garnet structure. This leads to the formation of solid-solution garnets and allows for a continuous variation of the local environment of Ce^{3+}. The modification of YAG:Ce^{3+} or LuAG:Ce^{3+} with the Ca^{2+}–Si^{4+} pair was inspired by naturally occurring mineral grossularite, $Ca_3Al_2(SiO_4)_3$.[39, 129] Kuru et al. were the first to investigate the solubility of Ca^{2+} and Si^{4+}.[128] Later, Katelnikovas reported $CaY_2Al_4SiO_{12}:Ce^{3+}$ and $CaLu_2Al_4SiO_{12}:Ce^{3+}$ with a blue-shifted Ce^{3+} emission in comparison to YAG:Ce and LuAG:Ce^{3+}. [39, 129] Similarly, incorporation of Mn^{2+}–Si^{4+} pairs into the aluminium garnets can be ascribed to the formation of solid solutions for the end members $Lu_3Al_5O_{12}$ and $Mn_3Al_2Si_3O_{12}$, which both possess the garnet structure. The solid solutions have the chemical formula of $Lu_{3-x-y}Mn_xAl_{5-x}Si_xO_{12}:yCe^{3+}$.[132] Furthermore, this strategy can enhance the relative intensity of the red Mn^{2+} component in the emission spectrum through Ce^{3+}-Mn^{2+} energy transfer. The emission spectra show that the incorporation of Mn^{2+} in garnet-type $Y_3Al_5O_{12}$ gives rise to broad band yellow–orange Mn^{2+} emission.[130-133]

$Lu_2CaMg_2Si_3O_{12}$ is another $(Ln,Me)_3(M,M')_5O_{12}$-based solid solution phosphors with garnet structure.[37-39] Lu^{3+}/Ca^{2+} ions are randomly located in eightfold dodecahedral sites with occupancies of 2/3 and 1/3, respectively. The Mg^{2+} ion is in the octahedral sites while Si^{4+} exclusively occupies the tetrahedral site. For example, $(Lu_{0.94}Ce_{0.06})_2CaMg_2Si_3O_{12}$ phosphor gives a luminescence band at ~605 nm when it is excited at 470 nm, an emission red shift of ~1700 cm^{-1} compared to YAG:Ce^{3+}. Setlur et al. reported a complete solid solution between the two silicate garnets $Ca_3Sc_2Si_3O_{12}$ and $Lu_2CaMg_2Si_3O_{12}$.[37] The emission shifts to higher energies with increasing Sc^{3+}/Ca^{2+} content. The Ce^{3+} emission color can be tuned over a surprisingly wide spectral range, from orange to blue-green emission by systematically replacing Sc^{3+} for Mg^{2+} and Ca^{2+} for Lu^{3+} in $Lu_{1.91-y}Ce_{0.09}Ca_{1+y}Mg_{2-y}Sc_ySi_3O_{12}$. The large blue shift when substituting Ca^{2+}–Sc^{3+} into $Lu_2CaMg_2Si_3O_{12}$ is explained by a combination of a smaller Ce^{3+} *5d* centroid shift and a smaller crystal field splitting because of the longer Ce^{3+}–O^{2-} bond length in the Ca-rich material. Note that the ionic radius of Ca^{2+} is much larger than that of Lu^{3+} (112 pm vs. 97.7 pm in VIII coordination).[134]

Furthermore, the observation of a blue shift when going from a smaller Lu^{3+} site to larger Ca^{2+} is different from the red shift observed in the LnAG garnets when the smaller Y^{3+} ion is replaced by a larger Tb^{3+} or Gd^{3+} ion. As discussed above, this is an unexpected shift that was explained by an increase in the $5d_1$-$5d_2$ splitting as a result of a larger tetragonal distortion. The complex behavior of the Ce^{3+} emission in garnets induced by cation substitution indicates illustrates how different effects influence the emission color of Ce^{3+} by affecting the position of the lowest 5d state. Structural characterization in combination with qualitative models and sometimes handwaving arguments can explain the behavior, but for a better understanding more quantitative modelling is required as will be discussed in the next section.

The crystal structure of $Mg_3Y_2(Ge,Si)_3O_{12}$ ($\{Y_2Mg\}[Mg]_2(Ge,Si)_3O_{12}$, MYGSG) belongs to what is called inverse garnets, where { }, [ ] and ( ) represents dodecahedral, octahedral and tetrahedral sites. New possibilities for the structural design of the new (inverse) garnet-type phosphors arise by using these inverse garnets.[4, 40, 135] The Ce^{3+} emission can be tuned varying the composition and especially by varying the Si-Ge ratio. The efficiency was found to be low which was explained by Shimizu et al. by the presence of different types of Ce^{3+} ions (low crystal field and high crystal field) due to the disorder in occupation of dodecahedral cation site.[135] As shown in Fig. 23a, their findings were based on a difference in the PLE spectrum and the photocurrent excitation spectrum (PCE). The PLE spectrum shows the $5d_1$ absorption band at lower energies than the PCE spectrum. This is explained by fast photoionization of Ce^{3+} ions on the low crystal field sites (CFS). As shown in Fig. 23(b), the small crystal field splitting places the $5d_1$ level at relative high energies, close to the conduction band leading to luminescence quenching by photoionization. For Ce^{3+} on a high CFS, the $5d_1$ level is pushed to lower energies and emission is observed. The quenching can be reduced by replacing Ge by Si. The bandgap for the silicate is higher than for the germanate and the higher energy of the conduction band reduces photoionization.

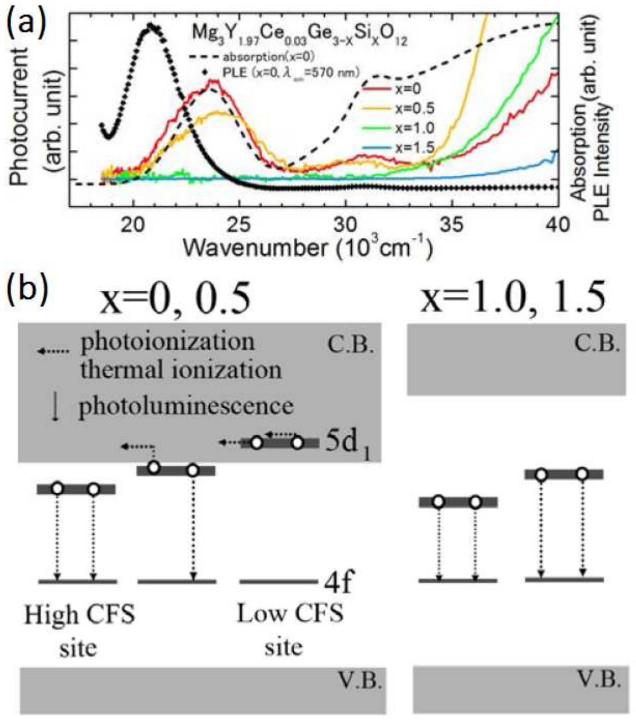

Fig. 23 (a) PCE, absorption and PLE spectra of $Mg_3Y_{1.97}Ce_{0.03}Ge_{3-x}Si_xO_{12}$:$Ce^{3+}$ (MYGSG:Ce^{3+}). Solid lines are the PCE spectra at 300 K. Dashed line and dots are the absorption spectrum and the PLE spectrum of $x = 0$ sample monitored at 570 nm. (b) Band scheme of MYGSG:Ce^{3+}. (Reprinted with permission from 135, copyright 2012, Wiley.)

3 Modelling of Luminescence in Relation to Structure

There is impressive amount of experimental data on the influence of cation substitution for the garnet host on the luminescence of Ce^{3+}. In Section 2 of this review only a selection of the experiments and insights gained have been described. The qualitative models used to explain the observations are often not conclusive. Especially when different effects have an opposite influence, the qualitative explanation assumes a stronger influence of the effect that can explain the observation versus the other, however without a quantitative justification. For example, both covalency/nephelauxetic effects and crystal field splitting result in a shift of the Ce^{3+} emission band. If cation substitution is expected to give rise a reduction in covalency but a larger crystal field splitting, both a blue shift and a red shift can be explained by assuming that either covalency or crystal field effects dominate. Without a reliable quantitative estimate, these explanations provide limited insight. For a better and more quantitative understanding it is important to be able to quantify the energy of excited states and changes in the energies as a result of variations in the local surroundings of the Ce^{3+} ion. In this section, a variety of modelling approaches will be discussed. Both modelling of the energy level structure of Ce^{3+} as well as the positions of the energy levels relative to the valence and conduction band of the host will be covered. In the past decade the field of modelling energy levels of lanthanide ions has seen impressive progress, enabled by the development of better models, increased computing power and a rather limited number dedicated researchers trying tackle this challenging problem.

Energy level calculations of $4f^{n-1}5d$ states of rare earth ions traditionally use parameter models.[136, 137] These models include parameters for the average energy for the 5*d* state, crystal field splitting of both the 4*f* state and 5*d* state, spin-orbit coupling and, for lanthanides with more than one 4*f* electron, also all the parameters for intraconfigurational 4*f* interactions in the $4f^{n-1}$ core[138] as well as interactions between the $4f^{n-1}$ core electrons and the 5*d* electron. With the parameter models both the positions of the $4f^{n-1}5d$ states as well as the intensities of $4f^{n} \rightarrow 4f^{n-1}5d$ transitions have been determined and show good agreement with experimental spectra.[127, 128]

For Ce^{3+} with only one 4*f* electron the situation is relatively simple. As there are no 4*f* electrons in the $4f^{n-1}5d$ excited state, the parameters for 4*f*-4*f* and 4*f*-5*d* interactions do not play a role. The energy level structure arises from the splitting of the 5*d* state determined by crystal field parameters, covalency effects and spin-orbit coupling. Brik et al. have performed energy level calculations for the $4f^1$ ground state and the 5*d* excited state of Ce^{3+} in YAG using a parameter model[139] The parameters that are used in the fitting procedure include an average energy off-set related to the position of the bary center of the 5*d* state and thus covalency/nephelauxetic effects. The crystal field parameters were determined for D_2 symmetry for Ce^{3+} on the dodecahedral site. The energy levels for the 5*d* states were modelled with the six relevant B^k_q crystal field parameters for D_2 symmetry. Parameters for spin-orbit coupling for the 5*d* state and for the 4*f* state are taken from the literature and fitting is done by adjusting the crystal field parameters. In Fig. 24 an example is shown of fitting the experimentally observed bands to the crystal field model using different parameter sets (I, II and II) [90] Based on the analysis, it is concluded that the peak observed at 260 nm is not from Ce^{3+} on the dodecahedral site but is related to a defect absorption, in line with the experimental observations of Tanner et al. Parameter set I in Fig. 24 gives the best agreement with the experimental observations, shown in the bottom part of Fig. The parameters used to obtain the fit are collected in Table 2.[140]

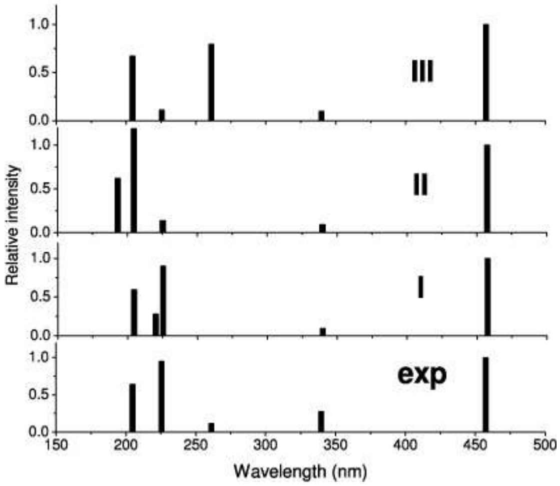

Fig. 24 Calculated wavelengths (positions bars) and relative intensities (height of bars) for transitions from the 4*f* ground state to the 5*d* excited states of YAG:Ce^{3+}. The experimental energies and intensities (lowest graph, exp) are obtained from the absorption spectra in ref. 141. The theoretically calculated positions and intensities were obtained from three different sets of fitting parameters shown in Table 2. (Reprinted with permission from ref. 90, copyright 2007, IOP Publishing.)

Table 2. Fitting parameters for the energy level structure of the 4*f* and 5*d* configurations of Ce^{3+} in YAG. Three sets of parameters are used (I, II and III) for the 5*d* crystal field splitting. ζ gives the spin-orbit coupling while the B^k_q parameters describe the crystal field splitting. See Ref. [141] for details.

4*f*				5*d*			
Parameter	cm^{-1}	Parameter	cm^{-1}	Parameter	I (cm^{-1})	II (cm^{-1})	III (cm^{-1})
ζ (ff)	647	B_0^6 (ff)	901	ζ (dd)	991	991	991
B_0^2 (ff)	−465	B_2^6 (ff)	307	B_0^2 (dd)	−6099	−1644	−8710
B_2^2 (ff)	−96	B_4^6 (ff)	2136	B_2^2 (dd)	−1259	−339	−1797
B_0^4 (ff)	−3739	B_6^6 (ff)	246	B_0^4 (dd)	−50 042	−58 960	−40 309
B_2^4 (ff)	−380	Δ (fd)	36 218	B_2^4 (dd)	−5374	−4197	−12 312
B_4^4 (ff)	1602			B_4^4 (dd)	19 626	18 569	18 164

The theoretical validation of the energy level structure is an important step towards quantitative understand of spectral shifts upon cation substitution. A quantitative correlation between the crystal field parameters and the red shift induced by Gd substitution in YAG:Ce^{3+} was provided by Liu et al.[142] Their analysis showed that especially the change in the B^4_4 crystal field parameter is responsible for the red shift induced by Gd substitution. Even though the parameter models provide quantitative insights, they are not capable of explaining how excited state wavefunctions change and how the local geometry varies as a result of cation substitution, nor do they provide a potential energy surface for the ground state and excited state. For these important insight *ab initio* calculations are required (*vide infra*).

In addition to modelling the 5*d* excited state also the splitting in the $4f^1$ ground configuration is important to explain features in the 5*d*-4*f* emission spectrum. Radiative decay to crystal field components of both the $^2F_{5/2}$ and $^2F_{7/2}$ multiplets are possible. Typically, for Ce^{3+} the $^2F_{5/2}$ and $^2F_{7/2}$ states are separated by ~2000 cm^{-1} arising from spin-orbit coupling. The crystal field splitting is of the $^2F_{5/2}$ and $^2F_{7/2}$ states is smaller than the spin-orbit splitting and as a result a typical double band structure is observed in emission. The two bands separated by ~2000 cm^{-1} correspond to transitions to the two states arising from spin-orbit splitting. However, for Ce^{3+} in YAG crystal field splitting is large, not only for the 5*d* state but also for the 4*f* states. The large 5*d* crystal field splitting gives rise to the anomalously long wavelength 5*d*-4*f* emission (yellow) for Ce^{3+} in an oxide, but is also responsible for a high energy crystal field component of the $^2F_{7/2}$ state. Experimental observations using IR spectroscopy in the 2000-4000 cm^{-1} region revealed a high energy (~3600 cm^{-1}) crystal field component of the $^2F_{7/2}$ multiplet and theoretical calculations confirmed a ~3500 cm^{-1} energy for the highest $^2F_{7/2}$ component in $Gd_3Ga_5O_{12}$ (GGG).[140] In YAG the highest crystal field component is calculated to be even above 4000 cm^{-1}.

In addition to parameter models describing the positions of the Ce^{3+} energy levels, other parameter models have been developed to locate the ground state and excited states of Ce^{3+} in the host band diagram. These band diagrams provide information on the positions of the 5*d* bands relative to the host VB and CB. Extensive work by Dorenbos has resulted in a model that describes the energy levels of 4*f* ground states and 5*d* excited states of lanthanides relative to the energies of the band edges of host material. Four parameters are used in this model. The first two parameters are the centroid shift ε_c of the 5*d* configuration (as discussed above, determined by covalency effects) and the depression D of the lowest 5*d* state (largely determined by the crystal field splitting). In addition to these parameters describing the Ce^{3+} energy level structure, the energy for the host bandgap is needed and is determined from the host exciton energy E_X. The final parameter is the energy for the charge transfer (CT) transition from the valence band to the lanthanide dopant which is used to locate the energy of the 4*f* ground state relative to the valence band. With these four parameters the relative energy of the 4*f* ground state and 5*d* excited state relative to the band edges can be determined. Information on the position of 4*f* and 5*d* states relative to the band edges of the host is especially important for understanding luminescence quenching processes based on thermally activated photoionization to the CB (electron) or VB (hole). Once the parameters have been determined for one lanthanide ion in a specific host, the parameters and thus energy positions for the other lanthanides in the same host can be predicted as there are well-established relations between these parameters for different lanthanides in the same host.

As an example, Fig. 25 shows the Vacuum Referred Binding Energy (VBRE) diagrams for Ce^{3+} in a variety of garnet hosts. The hosts include variation on the dodecahedral site (Gd, Y, Lu) and substitution on the octahedral/tetrahedral sites (all integer compositions Al_xGa_y from Al_5Ga_0 to Al_0Ga_5) for each of the three rare earth ions. In this diagram blue lines gives the Ce-energy levels, the 4*f* ground state is labelled (E_{4f}) and at higher energies the 5d_1 and 5d_2 states are shown. From vacuum UV excitation or absorption spectra the host excitation energy E_X can be determined (red dots in Fig. 25) and a constant energy difference is assumed between E_X and the conduction band edge (E_C). The energy difference between the valence band edge and 4*f* ground state is determined based on the energy of the charge transfer transition of Eu^{3+} in the various hosts. Note that the energy of the 4*f* ground state is constant in this diagram. This is rationalized by assuming that ionization of an electron from the inner 4*f* shell of the lanthanide ion to the vacuum level is constant and is not affected by the local surroundings as a result of the shielding of the 4*f* electrons by the filled outer 5*s* and 5*p* shells.

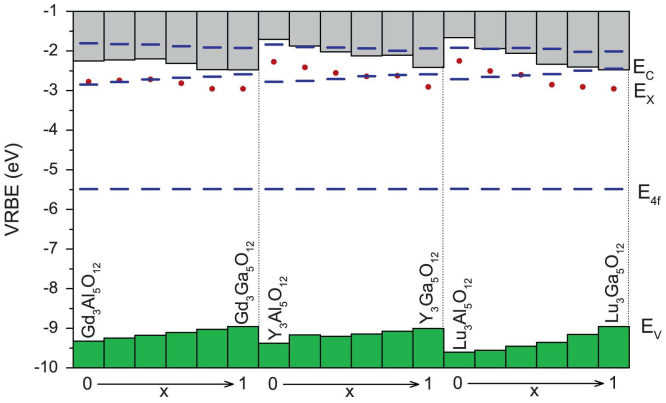

Fig. 25 Vacuum Referred Energy Binding (VRBE) diagrams for Ce^{3+} in a variety of garnet hosts. EV and EC denote the valence band and conduction band edge, E_{4f} (blue line) is the energy of the 4*f* ground state and E_X is the host exciton energy (red dots). The two lowest 5*d* crystals field levels of Ce^{3+} are indicated by the blue lines above the 4*f* ground state. (Reprinted with permission from ref. 80, copyright 2013, Elsevier.)

The VRBE diagrams are very useful as they have predictive value and also can be used to explain luminescence properties. For example, substitution of Al by Ga causes a shift of the 5d_1 level of Ce^{3+} to higher energies and simultaneous a downshift of E_C. This explains the lowering of the luminescence quenching temperature as the activation barrier for thermal ionization from the 5d_1 state to the conduction band is lowered. The higher quenching temperature for the 5*d* emission in YAG:Ce^{3+} compared to GAG:Ce^{3+} is also evident from the diagram as the gap between the 5d_1 level and the CB edge is much larger for Ce^{3+} in YAG than for Ce^{3+} in GAG. The accuracy of the VRBE diagrams is typically 0.2-0.5 eV and strongly depends on the quality of the experimental data. The most accurate data for energies of excited states are obtained from low temperature spectra and samples with very low dopant concentrations.[15, 143] Shifts of emission and absorption bands as a result of saturation effects, reabsorption and temperature broadening make the determination of the energies less accurate and this affects the accuracy of the VRBE diagrams. It is also crucial that experimental spectra are corrected correctly for the instrumental response to avoid errors in peak positions. It is clear that in the derivation of a VRBE diagram experimental data have to be critically evaluated.

Parameter models provide understanding of the energy level structure but do not give information on the wavefunctions and geometries in the ground or excited states, the change in equilibrium distance and the potential energy surface of the ground state and excited states. To truly understand the optical properties it is required to model the wavefunctions for ground and excited state using first principle methods. This is an ambitious goal for lanthanide ions since a large number of orbitals needs to be included in the calculations and both relativistic effects and spin-orbit coupling cannot be neglected. This makes the calculations computationally demanding and it requires dedicated expertise. In the past decade however, strong progress has been realized in providing understanding in the optical properties of lanthanide ions using *ab initio* methods.[144-149] Garnets have served as model systems and calculations have been done to understand the basic luminescence properties (model excitation and emission spectra, Stokes shift) as well as the observed spectral changes upon cation substitution.

One type of model that is successfully applied for *ab initio* calculations for YAG:Ce^{3+} uses complete-active-space self-consistent-field (CASSCF) and second-order many-body perturbation theory (CASPT2) methods including relativistic ab initio model potential (AIMP) embedded cluster Hamiltonians with spin–orbit coupling.[150] Typically, the calculations involve a cluster of the Ce^{3+} ion and nearest oxygen ligands and possibly also the next nearest cations. The geometry of the cluster is obtained from crystallographic data and can be optimized using Density Functional Theory (DFT). An example of a cluster is shown in Fig. 26. The cluster is embedded in a potential that accounts for the effects of the host. A large basis set of wavefunctions of the ions in the cluster is used. Together with the geometry, this is the only input in the calculations. There are no fitting parameters. First calculations are done with a spin–orbit free Hamiltonian, taking into account bonding and static correlation effects. In the next step second-order perturbation theory calculations are performed including dynamic correlation effects of the 5*s*, 5*p*, 4*f* and 5*d* electrons of Ce and the 2*s* and 2*p* electrons of O. Typically, a program as MOLCAS is used. In the final phase the full Hamiltonian includes the spin–orbit coupling operator and spin–orbit configuration interaction. The calculations are very complex and only a few groups worldwide have the expertise to do these calculations.

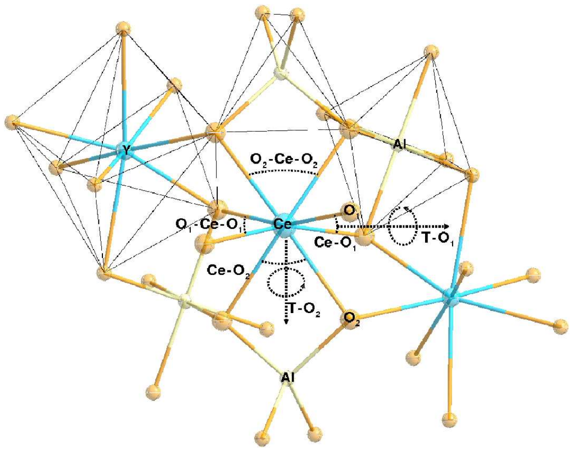

Fig. 26 Cluster $(CeO_8)^{13-}$ with the nearest neighbor cations and anions arranged in (AlO_4) tetrahedral, (AlO_6) octahedra and (YO_8) dodecahedra. Bond angles and torsion angles have been optimized. (Reprinted with permission from ref. 150, copyright 2008, Elsevier.)

The absorption and emission spectra that are predicted based on the *ab initio* calculations for YAG:Ce^{3+} are shown in Fig. 27.[150] The crystal field splitting for both the 5*d* excited state and 4*f* ground state are well reproduced by the calculation. Comparison with the experimentally measured positions (see for experimental data Fig. 24, bottom 'exp') shows that the absolute energies calculated for the 5*d* states are shifted by about 2000 - 3000 cm^{-1} to higher energies. For the 4*f* ground state the high energy crystal field component of the higher energy $^2F_{7/2}$ level (around 4000 cm^{-1}) is also well-reproduced. The transition from the 5*d* state to this crystal field component is visible as a weak shoulder around 19 500 cm^{-1} in the 5*d*-4*f* emission spectrum (Fig. 27, bottom). Again, the absolute energy of the emission is overestimated, by about 4000 cm^{-1}. The larger deviation in emission compared to absorption reflects that the Stokes shift is underestimated. The calculated Stokes shift is only 700 cm^{-1} whereas low temperature measurements on very dilute YAG: 0.03%Ce^{3+} has provided an experimentally determined Stokes shift of just over 2000 cm^{-1}. It is evident that the *ab initio* calculations do not take into account all effects and that probably the actual relaxation in the excited state is stronger than calculated. In spite of the differences with experimental results the discrepancy is getting smaller and the progress is encouraging. The overall spectral features (both intensities and spectral positions) are well reproduced without any fitting parameter. The calculations provide insight in the nature of excited states and geometry changes in the transition from ground state to excited state.

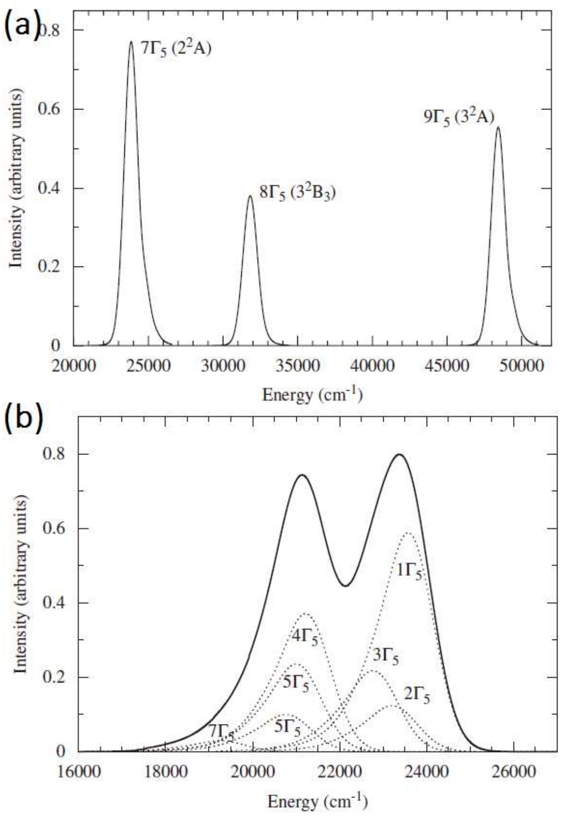

Fig. 27 Theoretically calculated absorption (a) and emission (b) spectra for Ce^{3+} in YAG using ab initio calculations. For details, see text and ref. 150. (Reprinted with permission from ref. 150, copyright 2008, Elsevier.)

Using *ab initio* calculations it is also possible to model the shift in spectral properties induced by cation substitution. Both the effect of substitution of Y by La and substitution of Al by Ga have been modelled by the group of Seijo and Barandiaran.[151, 152] In Fig. 28 the Ce-La cluster is depicted. The *ab initio* calculations reproduce the experimental observations that upon replacing the smaller Y^{3+} with a larger La^{3+} ion, the Ce^{3+} emission from the 5d_1 states shifts to lower energies (red shift) while the 5d_2 state shifts to higher energies (blue shift). Not only do *ab initio* calculations reproduce these results, they also give insight in the origin of the shift. The substitution of La in neighboring sites leads to a local expansion of the Ce-O distances which gives rise to a small blue shift, in line with classical models for crystal field models. However, electronic effects give a larger contribution to an increase in crystal field splitting, which together with a smaller 4*f*-5*d* centroid difference explains the observed redshift.[151] Similar calculations for Al-Ga substitution reproduce the experimentally observed blue shift.[152] Again, the calculations provide insight in the origin for the shift that cannot be obtained from parameter models or handwaving arguments. One might expect a red shift based on an increased covalency as Al is replaced by the more covalent Ga. The calculations show that the blue shift is almost completely due to an expansion of the Ce^{3+} surroundings induced by the Ga substitutions that reduces the crystal field splitting. The 4*f*-5*d* centroid separation is not affected and there is no direct electronic effect of Ga. The closer proximity of La-Ce compared to Ga-Ce explains why an electronic effect is present for La substitution and not for Ga substitution.

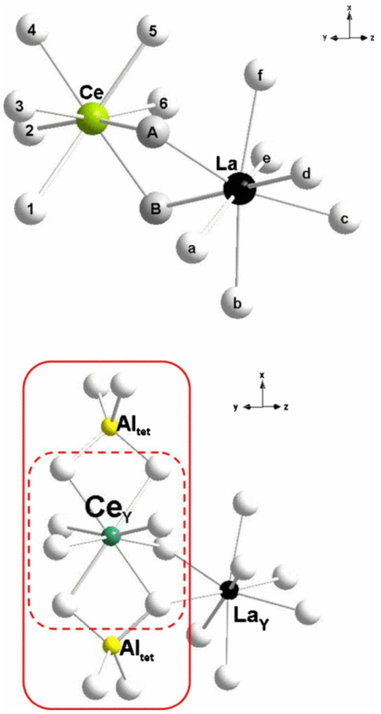

Fig. 28 Geometry of La-Ce cluster in YAG:Ce^{3+} with La substitution (see ref. 151 for details). (Reprinted with permission from ref. 151, copyright 2010, American Physical Society.)

Band structure calculations have gained popularity in the past decade and especially DFT based methods are widely applied to calculate band energies and density of states for crystalline materials (insulators and semiconductors). For the garnets DFT calculations have been done to provide insight in the luminescence properties and to provide a quantitative validation of the band diagrams in the Dorenbos model. Similar to first principles *ab initio* calculations, DFT calculations provide insight in the nature of excited states and the origin of changes in the electronic structure that cannot be obtained from parameter models.

As an example, Fig. 29 shows band structure calculations for YAG, YAG:Ce and (Y,Gd)AG. The electronic band structure (BS), density of states (DOS), partial density of states (PDOS), and charge deformation density (CDD) were calculated using DFT. As a starting point for the calculations the geometry was optimized using the generalized gradient approximation. The calculations show that the bandgap decreases from 6.505 eV for pure YAG to 6.358 eV for $(Y_{2.94}Ce_{0.06})Al_5O_{12}$. Addition of Gd decreases the bandgap, to 6.206 eV for $(Y_{0.75}Gd_{0.25})_3Al_5O_{12}$ and to 6.071 eV for $(Y_{0.25}Gd_{0.75})_3A_{l5}O_{12}$. This trend is consistent with the Dorenbos diagrams (see e.g. Fig. 25) and experimental results showing a decrease in bandgap upon substitution of Y by Gd. The DFT calculations also provide insight in the origin of the change in bandgap. Supported by structural characterization of Y-O and Gd-O distances as a function of Gd concentration, the calculations of the PDOS reveal a stronger hybridization for the O and Gd orbitals than for the O and Y orbitals. The stronger mixing of orbitals gives rise to a reduction in bandgap. XRD and EXAFS data indicate that the Gd-O bond length hardly increases upon substitution of Y by Gd, in spite of the larger ionic radius of Gd^{3+}. The resulting compressive stress is related to the increase in hybridization. The increase in hybridization upon raising the Gd concentration also causes an increase in crystal field splitting for Ce^{3+} substituted on the dodecahedral site. This explanation is consistent with the *ab initio* calculations discussed above that showed an increase in crystal field splitting upon La substitution through electronic effects.

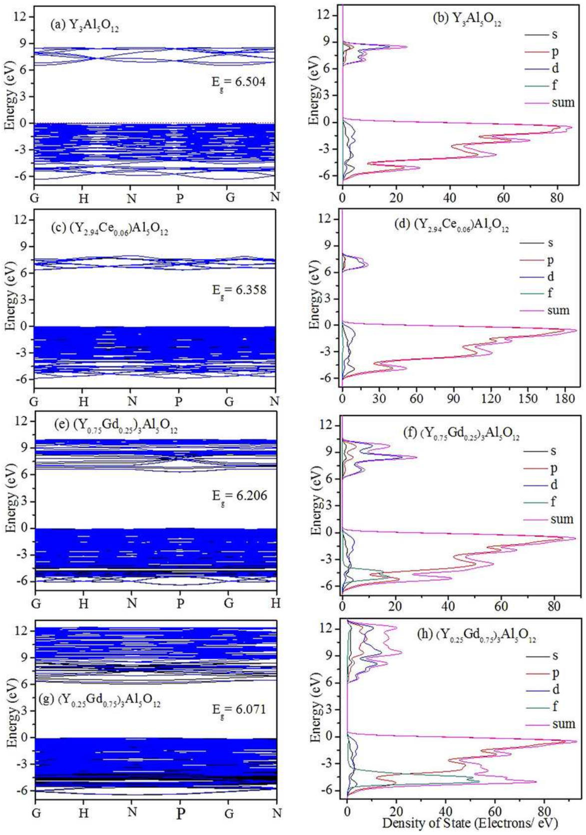

Fig. 29 Band structure diagrams (left) and density of state, including partial density of states from DFT calculations for $Y_3Al_5O_{12}$, $(Y_{2.94}Ce_{0.06})Al_5O_{12}$, $(Y_{0.75}Gd_{0.25})_3Al_5O_{12}$ and $(Y_{0.25}Gd_{0.75})_3Al_5O_{12}$. For details see ref.[153]. (Reprinted with permission from ref. 153, Copyright 2015, Nature Publishing group.)

It is expected that further development of more accurate models will continue as the rapid increase in computing power allows for larger basis sets of orbitals and faster calculations. The fruitful interaction between experiment and theory will help to improve the models that are used for calculating the spectroscopic properties of ions in solids. It is evident that the garnet host is a model system for testing theoretical models as it has high symmetry (helpful in reducing computation time) and offers great flexibility in changing host properties through cation substitution on three different sites. At present, theoretical models are increasingly capable of providing insight in excited state configurations and effects that are responsible for changes in luminescence properties such as excitation and emission wavelengths and thermal quenching temperature. The results presented here for YAG:Ce^{3+} are illustrative for the capability and usefulness of the presently existing models. In the future more accurate calculations of excitation and emission bands and Stokes shifts of emission will be realized. The final goal, reliable calculations predicting all of the optical properties before a luminescent material is made is still far away but may be reached one day.

4 Conclusion and outlook

Understanding of the "Structure-Property Relationship" plays an important role in the development of the new functional materials and providing new physical insights. Crystal chemistry strategies are the basis for the tuning and understanding of material properties, as well as the discovery and structural design of new phosphor materials for emerging applications.[154] Garnets are an important class inorganic minerals, with a simple cubic crystal structure and yet a complex chemical composition. Garnets doped with Ce^{3+} have been demonstrated in the past to form an unusually flexible class of luminescent materials. Cation substitution on three different cation sites (dodecahedral, octahedral or tetrahedral) allows for tuning the optical properties. This makes Ce^{3+}-doped garnets the luminescent material that has been (and still is) applied in the largest variety of applications, including cathode ray tubes, fluorescent lamps, dosimeters, afterglow materials, scintillators and, most prominently, in white light LEDs.

In this review we have analyzed how the variation in structure and chemical composition relates to the luminescence properties of Ce^{3+}-doped garnets. Since the surprising discovery of yellow emission from Ce^{3+} in an oxide, YAG, Ce^{3+}-doped garnets serve as a model system enabling the design of new inorganic functional materials that can be tailored for a specific application. In the past decades, many Ce^{3+}-doped garnets have been studied in detail in order to improve e.g. the color rendering index, structural stability, x-ray absorption, thermal quenching of luminescence, afterglow characteristics and so on.

Several rules relating to crystal chemistry strategies for modification of optical properties have been demonstrated and are discussed in relation to theoretical models (both parameter based models and true *ab initio* calculations) for the optical properties of Ce^{3+}. A red-shifted Ce^{3+} emission (compared to YAG:Ce^{3+}) can be observed when the radius of ions substituting on the dodecahedral site is larger than Y^{3+} while the blue-shift happens with the increasing radius of ions substituting on the M and M' sites. Both effects can be explained by theoretical calculations. Changes in the alignment of the 5*d* levels of Ce^{3+} relative to the host band edges can be used to understand thermal quenching and afterglow behavior. The progress on the insight in the relation between chemical composition and luminescence properties of Ce^{3+} in garnets will guide future research on new Ce^{3+}-doped garnets and more in general it will help the development of new luminescent materials with tailored optical properties.

Acknowledgements

The present work was supported by the National Natural Science Foundations of China (Grant No. No.51572023, No.51272242), the Program for New Century Excellent Talents in University of Ministry of Education of China (NCET-12-0950), the Funds of the State Key Laboratory of Rare Earth Resource Utilization, Changchun Institute of Applied Chemistry, CAS (RERU2015022), the Funds of the State Key Laboratory of New Ceramics and Fine Processing, Tsinghua University (KF201306), and Fundamental Research Funds for the Central Universities (FRF-TP-15-003A2).

References

1. G. Blasse and A. Bril, *Appl. Phys. Lett.*, 1967, **11**, 53-55.
2. J. Geusic, H. Marcos and L. Van Uitert, *Appl. Phys. Lett.*, 1964, **4**, 182-184.
3. T. Yanagida, H. Takahashi, T. Ito, D. Kasama, T. Enoto, M. Sato, S. Hirakuri, M. Kokubun, K. Makishima and T. Yanagitani, *IEEE Trans. Nucl. Sci.*, 2005, **52**, 1836-1841.
4. J. L. Wu, G. Gundiah and A. Cheetham, *Chem. Phys. Lett.*, 2007, **441**, 250-254.
5. M. Nikl, A. Yoshikawa, K. Kamada, K. Nejezchleb, C. Stanek, J. Mares and K. Blazek, *Prog. Cryst. Growth Charact. Mater.*, 2013, **59**, 47-72.
6. Z. Xia, Z. Xu, M. Chen and Q. Liu, *Dalton Trans.*, 2016, **45**, 11214-11232.
7. G. Li, Y. Tian, Y. Zhao and J. Lin, *Chem. Soc. Rev.*, 2015, **44**, 8688-8713.
8. S. Ye, F. Xiao, Y. X. Pan, Y. Y. Ma and Q. Y. Zhang, *Materials Science & Engineering R-Reports*, 2010, **71**, 1-34.
9. A. Nakatsuka, A. Yoshiasa and T. Yamanaka, *Acta Crystallogr., Sect. B: Struct. Sci*, 1999, **55**, 266-272.
10. G. Menzer, *Zeitschrift für Kristallographie-Crystalline Materials*, 1929, **69**, 300-396.
11. J. T. C. van Kemenade, G. H. M. Siebers, J. J. Heuvelmans, J. T. W. deHair and J. W. Vrugt, U.S. Patents., 4 727 283, 1988.
12. E. Zych, C. Brecher, A. Wojtowicz and H. Lingertat, *J. Lumin.*, 1997, **75**, 193-203.
13. C. R. Ronda, *Luminescence: from theory to applications*, John Wiley & Sons, 2007.
14. P. Von Dollen, S. Pimputkar and J. S. Speck, *Angewandte Chemie International Edition*, 2014, **53**, 13978-13980.
15. V. Bachmann, C. Ronda and A. Meijerink, *Chem. Mater.*, 2009, **21**, 2077-2084.
16. Y. Shimizu, K. Sakano, Y. Noguchi and T. Moriguchi, *Journal*, 1999.
17. G. Fasol and S. Nakamura, *Journal*, 1997.
18. R. Mueller‐Mach, G. Mueller, M. R. Krames, H. A. Höppe, F. Stadler, W. Schnick, T. Juestel and P. Schmidt, *physica status solidi (a)*, 2005, **202**, 1727-1732.
19. N. C. George, K. A. Denault and R. Seshadri, *Annu. Rev. Mater. Res.*, 2013, **43**, 481-501.
20. N. J. Cherepy, J. D. Kuntz, T. M. Tillotson, D. T. Speaks, S. A. Payne, B. Chai, Y. Porter-Chapman and S. E. Derenzo, *Nucl. Instrum. Methods Phys. Res., Sect. A*, 2007, **579**, 38-41.
21. X. Liu, X. Wang and W. Shun, *physica status solidi (a)*, 1987, **101**, K161-K165.
22. S. Zhang, L. Chengyu, P. Ran, L. Jiang, S. Lili and S. Qiang, *J. Rare Earths*, 2011, **29**, 426-430.
23. D. Mateika, E. Völkel and J. Haisma, *J. Cryst. Growth*, 1990, **102**, 994-1013.
24. L. Chen, C. C. Lin, C. W. Yeh and R. S. Liu, *Materials*, 2010, **3**, 2172-2195.
25. C. H. Huang and T. M. Chen, *Opt. Express*, 2010, **18**, 5089-5099.
26. Y. Shimomura, T. Honma, M. Shigeiwa, T. Akai, K. Okamoto and N. Kijima, *J. Electrochem. Soc.*, 2007, **154**, J35-J38.
27. Y. Shimomura, T. Kurushima, M. Shigeiwa and N. Kijima, *J. Electrochem. Soc.*, 2008, **155**, J45-J49.
28. F. Kummer, F. Zwaschka, A. Ellens, A. Debray and G. Waitl, *International Patent Application No.: WO*, 2001, **1**, 08452.
29. Y. Chen, J. Wang, M. Gong and Q. Su, *J. Solid State Chem.*, 2007, **180**, 1165-1170.
30. P. Yadav, C. Joshi and S. Moharil, *J. Lumin.*, 2013, **136**, 1-4.
31. H. C. Jung, J. Y. Park, G. Raju, B. C. Choi, J. H. Jeong and B. K. Moon, *J. Am. Ceram. Soc.*, 2011, **94**, 551-555.
32. A. A. Setlur, W. J. Heward, M. E. Hannah and U. Happek, *Chem. Mater.*, 2008, **20**, 6277-6283.
33. X. Wang, G. Zhou, H. Zhang, H. Li, Z. Zhang and Z. Sun, *J. Alloys Compd.*, 2012, **519**, 149-155.
34. A. Katelnikovas, T. Bareika, P. Vitta, T. Jüstel, H.

Winkler, A. Kareiva, A. Žukauskas and G. Tamulaitis, *Opt. Mater.*, 2010, **32**, 1261-1265.

35. A. Katelnikovas, H. Winkler, A. Kareiva and T. Jüstel, *Opt. Mater.*, 2011, **33**, 992-995.

36. A. Katelnikovas, J. Jurkevičius, K. Kazlauskas, P. Vitta, T. Jüstel, A. Kareiva, A. Žukauskas and G. Tamulaitis, *J. Alloys Compd.*, 2011, **509**, 6247-6251.

37. A. A. Setlur, W. J. Heward, Y. Gao, A. M. Srivastava, R. G. Chandran and M. V. Shankar, *Chem. Mater.*, 2006, **18**, 3314-3322.

38. M. S. Kishore, N. P. Kumar, R. G. Chandran and A. Setlur, *Electrochem. Solid-State Lett.*, 2010, **13**, J77-J80.

39. A. Katelnikovas, J. Plewa, D. Dutczak, S. Möller, D. Enseling, H. Winkler, A. Kareiva and T. Jüstel, *Opt. Mater.*, 2012, **34**, 1195-1201.

40. Z. Jiang, Y. Wang and L. Wang, *J. Electrochem. Soc.*, 2010, **157**, J155-J158.

41. Z. Pan, W. Li, Y. Xu, Q. Hu and Y. Zheng, *RSC Advances*, 2016, **6**, 20458-20466.

42. H. Ji, L. Wang, M. S. Molokeev, N. Hirosaki, R. Xie, Z. Huang, Z. Xia, O. M. ten Kate, L. Liu and V. V. Atuchin, *J. Mater. Chem. C*, 2016, **4**, 6855-6863.

43. X. Gong, J. Huang, Y. Chen, Y. Lin, Z. Luo and Y. Huang, *Inorg. Chem.*, 2014, **53**, 6607-6614.

44. J. Zhong, W. Zhuang, X. Xing, R. Liu, Y. Li, Y. Liu and Y. Hu, *The Journal of Physical Chemistry C*, 2015, **119**, 5562-5569.

45. X. Ding, G. Zhu, W. Geng, Q. Wang and Y. Wang, *CrystEngComm*, 2015, **17**, 3235-3242.

46. M. Nikl, J. Mares, N. Solovieva, J. Hybler, A. Voloshinovskii, K. Nejezchleb and K. Blazek, *physica status solidi (a)*, 2004, **201**, R41-R44.

47. M. Nikl, A. Yoshikawa, A. Vedda and T. Fukuda, *J. Cryst. Growth*, 2006, **292**, 416-421.

48. Y. Wu and G. Ren, *CrystEngComm*, 2013, **15**, 4153-4161.

49. K. Kamada, T. Endo, K. Tsutumi, T. Yanagida, Y. Fujimoto, A. Fukabori, A. Yoshikawa, J. Pejchal and M. Nikl, *Crystal Growth & Design*, 2011, **11**, 4484-4490.

50. J. M. Ogiegło, A. Katelnikovas, A. Zych, T. Jüstel, A. Meijerink and C. R. Ronda, *The Journal of Physical Chemistry A*, 2013, **117**, 2479-2484.

51. J. Ueda, K. Aishima, S. Nishiura and S. Tanabe, *Appl. Phys Express*, 2011, **4**, 042602.

52. Y. Luo and Z. Xia, *The Journal of Physical Chemistry C*, 2014, **118**, 23297-23305.

53. H. Lin, J. Xu, Q. Huang, B. Wang, H. Chen, Z. Lin and Y. Wang, *ACS Appl. Mater. Interf.*, 2015, **7**, 21835-21843.

54. W. Holloway and M. Kestigian, *JOSA*, 1969, **59**, 60-63.

55. S.-J. Liu, T.-J. Peng, Z. Song, L. Bian, G.-B. Song and Q.-L. Liu, *Chinese Physics B*, 2014, **23**, 048106.

56. Z. Song, R. Zu, X. Liu, L. He and Q. Liu, *Cryst. Res. Technol.*, 2016, **51**, 239-242.

57. Y.-B. Chen, Z.-B. Tang, X.-S. Xu, D.-H. Feng, Z.-Z. Wang and Z.-Q. Liu, *RSC Advances*, 2016, **6**, 43916-43923.

58. J. Zhong, W. Zhuang, X. Xing, R. Liu, Y. Li, Y. Zheng, Y. Hu and H. Xu, *RSC Advances*, 2016, **6**, 2155-2161.

59. H. Ji, L. Wang, M. S. Molokeev, N. Hirosaki, Z. Huang, Z. Xia, M. Otmar, L. Liu and R. Xie, *J. Mater. Chem. C*, 2016, **4**, 2359-2366.

60. D. J. Robbins, B. Cockayne, J. L. Glasper and B. Lent, *J. Electrochem. Soc.*, 1979, **126**, 1213-1220.

61. D. J. Robbins, B. Cockayne, B. Lent, C. N. Duckworth and J. L. Glasper, *Physical Review B*, 1979, **19**, 1254-1269.

62. F. Andreola, L. Barbieri, A. Corradi and I. Lancellotti, *J. Eur. Ceram. Soc.*, 2007, **27**, 1623-1629.

63. M. Nikl and A. Yoshikawa, *Advanced Optical Materials*, 2015, **3**, 463-481.

64. M. Nikl, A. Yoshikawa, K. Kamada, K. Nejezchleb, C. R. Stanek, J. A. Mares and K. Blazek, *Prog. Cryst. Growth Charact. Mater.*, 2013, **59**, 47-72.

65. K. L. Tom, *Physics in Medicine and Biology*, 2008, **53**, R287.

66. A. Ikesue, T. Kinoshita, K. Kamata and K. Yoshida, *J. Am. Ceram. Soc.*, 1995, **78**, 1033-1040.

67. E. Zych, C. Brecher, A. J. Wojtowicz and H. Lingertat, *J. Lumin.*, 1997, **75**, 193-203.

68. A. Ikesue and Y. L. Aung, *Nat Photon*, 2008, **2**, 721-727.

69. J. McKittrick and L. E. Shea-Rohwer, *J. Am. Ceram. Soc.*, 2014, **97**, 1327-1352.

70. T. Tomiki, H. Akamine, M. Gushiken, Y. Kinjoh, M. Miyazato, T. Miyazato, N. Toyokawa, M. Hiraoka, N. Hirata and Y. Ganaha, *J. Phys. Soc. Jpn.*, 1991, **60**, 2437-2445.

71. P. Dorenbos, *J. Lumin.*, 2000, **91**, 91-106.

72. P. Dorenbos, *J. Lumin.*, 2000, **91**, 155-176.

73. D. Robbins, *J. Electrochem. Soc.*, 1979, **126**, 1550-1555.

74. P. Dorenbos, *Physical Review B*, 2000, **62**, 15640.

75. P. Dorenbos, *Physical Review B*, 2000, **62**, 15650.

76. P. Dorenbos, *Physical Review B*, 2001, **64**, 125117.

77. P. Dorenbos, *Physical Review B*, 2002, **65**, 235110.

78. P. Dorenbos, *J. Alloys Compd.*, 2002, **341**, 156-159.

79. P. Dorenbos, *J. Lumin.*, 2002, **99**, 283-299.

80. P. Dorenbos, *J. Lumin.*, 2013, **134**, 310-318.

81. L. Chen, C.-C. Lin, C.-W. Yeh and R.-S. Liu, *Materials*, 2010, **3**, 2172-2195.

82. J. Solé, L. Bausa and D. Jaque, *An introduction to the optical spectroscopy of inorganic solids*, John Wiley & Sons, 2005.

83. R.-J. Xie, Y. Q. Li, N. Hirosaki and H. Yamamoto, *Nitride phosphors and solid-state lighting*, CRC Press, 2016.

84. P. Dorenbos, J. Andriessen and C. Van Eijk, *J. Solid State Chem.*, 2003, **171**, 133-136.

85. P. D. Rack and P. H. Holloway, *Materials Science and Engineering: R: Reports*, 1998, **21**, 171-219.

86. J. Ueda, K. Aishima and S. Tanabe, *Opt. Mater.*, 2013, **35**, 1952-1957.

87. A. Setlur and A. Srivastava, *Opt. Mater.*, 2007, **29**, 1647-1652.

88. L. Zhang, J. Zhang, X. Zhang, Z. Hao, H. Zhao and Y. Luo, *ACS Appl. Mater. Interf.*, 2013, **5**, 12839-12846.

89. Y. C. Wu, D. Y. Wang, T. M. Chen, C. S. Lee, K. J. Chen and H. C. Kuo, *ACS Appl. Mater. Interf.*, 2011, **3**, 3195-3199.

90. P. A. Tanner, L. Fu, L. Ning, B.-M. Cheng and M. G. Brik, *Journal of Physics: Condensed Matter*, 2007, **19**, 216213.

91. Q. Shao, Y. Dong, J. Jiang, C. Liang and J. He, *J. Lumin.*, 2011, **131**, 1013-1015.

92. K. Li and C. Shen, *Optik-International Journal for Light and Electron Optics*, 2012, **123**, 621-623.

93. R. Hansel, S. Allison and G. Walker, *J. Mater. Sci.*, 2010, **45**, 146-150.

94. C.-C. Chiang, M.-S. Tsai and M.-H. Hon, *J. Electrochem. Soc.*, 2007, **154**, J326-J329.

95. C.-C. Chiang, M.-S. Tsai and M.-H. Hon, *J. Electrochem. Soc.*, 2008, **155**, B517-B520.

96. Y. Zorenko, V. Gorbenko, I. Konstankevych, B. Grinev and M. Globus, *Nucl. Instrum. Methods Phys. Res., Sect. A*, 2002, **486**, 309-314.

97. K. Kamada, T. Yanagida, T. Endo, K. Tsutumi, M. Yoshino, J. Kataoka, Y. Usuki, Y. Fujimoto, A. Fukabori and A. Yoshikawa, *J. Cryst. Growth*, 2012, **352**, 91-94.

98. V. Babin, V. Gorbenko, A. Krasnikov, A. Makhov, M. Nikl, S. Zazubovich and Y. Zorenko, *Radiat. Meas.*, 2010, **45**, 415-418.

99. J. M. Ogiegło, A. Zych, K. V. Ivanovskikh, T. Jüstel, C. R. Ronda and A. Meijerink, *The Journal of Physical Chemistry A*, 2012, **116**, 8464-8474.

100. H. T. Kim, J. H. Kim, J.-K. Lee and Y. C. Kang, *Mater. Res. Bull.*, 2012, **47**, 1428-1431.

101. M. Batentschuk, A. Osvet, G. Schierning, A. Klier, J. Schneider and A. Winnacker, *Radiat. Meas.*, 2004, **38**, 539-

543.

102. Y. Zorenko, T. Voznyak, V. Vistovsky, T. Zorenko, S. Nedilko, M. Batentschuk, A. Osvet, A. Winnacker, G. Zimmerer and V. Kolobanov, *Radiat. Meas.*, 2007, **42**, 648-651.

103. M.-S. Tsai, G.-M. Liu and S.-L. Chung, *Mater. Res. Bull.*, 2008, **43**, 1218-1222.

104. M. Nazarov, J. Sohn and C. Yoon, *Opt. Mater.*, 2008, **30**, 1387-1392.

105. A. Setlur, J. Shiang and C. Vess, *The Journal of Physical Chemistry C*, 2011, **115**, 3475-3480.

106. C. Chiang, M. Tsai and M.-H. Hon, *J. Alloys Compd.*, 2007, **431**, 298-302.

107. J. Li, J. G. Li, Z. Zhang, X. Wu, S. Liu, X. Li, X. Sun and Y. Sakka, *J. Am. Ceram. Soc.*, 2012, **95**, 931-936.

108. Q. Y. Shao, Y. Dong, J. Q. Jiang, C. Liang and J. H. He, *J. Lumin.*, 2011, **131**, 1013-1015.

109. K. V. Ivanovskikh, J. M. Ogiegło, A. Zych, C. R. Ronda and A. Meijerink, *ECS J. Solid State Sci. Technol.*, 2013, **2**, R3148-R3152.

110. J. Ueda, S. Tanabe and T. Nakanishi, *J. Appl. Phys.*, 2011, **110**, 053102.

111. J. Ueda, P. Dorenbos, A. J. Bos, A. Meijerink and S. Tanabe, *The Journal of Physical Chemistry C*, 2015, **119**, 25003-25008.

112. K. Kamada, T. Yanagida, T. Endo, K. Tsutumi, Y. Usuki, M. Nikl, Y. Fujimoto, A. Fukabori and A. Yoshikawa, *J. Cryst. Growth*, 2012, **352**, 88-90.

113. M. Tyagi, F. Meng, M. Koschan, S. B. Donnald, H. Rothfuss and C. L. Melcher, *J. Phys. D: Appl. Phys.*, 2013, **46**, 475302.

114. Y. Wu, M. Nikl, V. Jary and G. Ren, *Chem. Phys. Lett.*, 2013, **574**, 56-60.

115. T. Kanai, M. Satoh and I. Miura, *J. Am. Ceram. Soc.*, 2008, **91**, 456-462.

116. K. Van den Eeckhout, P. F. Smet and D. Poelman, *Materials*, 2010, **3**, 2536-2566.

117. T. Tien, E. Gibbons, R. DeLosh, P. Zacmanidis, D. Smith and H. Stadler, *J. Electrochem. Soc.*, 1973, **120**, 278-281.

118. J. Robertson, M. Van Tol, W. Smits and J. Heynen, *Philips J. Res.*, 1981, **36**, 15-30.

119. M. C. Maniquiz, K. Y. Jung and S. M. Jeong, *J. Electrochem. Soc.*, 2011, **158**, H697-H703.

120. A. Katelnikovas, H. Bettentrup, D. Uhlich, S. Sakirzanovas, T. Jüstel and A. Kareiva, *J. Lumin.*, 2009, **129**, 1356-1361.

121. Y. Jia, Y. Huang, N. Guo, H. Qiao, Y. Zheng, W. Lv, Q. Zhao and H. You, *RSC Adv.*, 2012, **2**, 2678-2681.

122. H. Luo, J. Liu, X. Zheng, B. Xu, Y. Lu, L. Han, K. Ren and X. Yu, *J. Am. Ceram. Soc.*, 2012, **95**, 3582-3587.

123. M. Sopicka-Lizer, D. Michalik, J. Plewa, T. Juestel, H. Winkler and T. Pawlik, *J. Eur. Ceram. Soc.*, 2012, **32**, 1383-1387.

124. Y. Liu, X. Zhang, Z. Hao, X. Wang and J. Zhang, *J. Mater. Chem.*, 2011, **21**, 6354-6358.

125. J. Qiao, J. Zhang, X. Zhang, Z. Hao, W. Deng, Y. Liu, L. Zhang, L. Zhang, H. Zhao and J. Lin, *Opt. Lett.*, 2013, **38**, 884-886.

126. B. Mill, E. Belokoneva, M. Simonov and N. Belov, *J. Struct. Chem.*, 1977, **18**, 321-323.

127. Y. Liu, X. Zhang, Z. Hao, Y. Luo, X. Wang and J. Zhang, *J. Mater. Chem.*, 2011, **21**, 16379-16384.

128. Y. Kuru, E. Onur Savasir, S. Zeynep Nergiz, C. Oncel and M. Ali Gulgun, *physica status solidi (c)*, 2008, **5**, 3383-3386.

129. A. Katelnikovas, S. Sakirzanovas, D. Dutczak, J. Plewa, D. Enseling, H. Winkler, A. Kareiva and T. Jüstel, *J. Lumin.*, 2013, **136**, 17-25.

130. Z. Mu, Y. Hu, Y. Wang, H. Wu, C. Fu and F. Kang, *J. Lumin.*, 2011, **131**, 676-681.

131. Z. Mu, Y. Hu, H. Wu, C. Fu and F. Kang, *Physica B*, 2011, **406**, 864-868.

132. Y. Jia, Y. Huang, Y. Zheng, N. Guo, H. Qiao, Q. Zhao, W. Lv and H. You, *J. Mater. Chem.*, 2012, **22**, 15146-15152.

133. Y. Jia, N. Guo, Y. Zheng, H. Qiao, W. Lv, Q. Zhao and H. You, *ChemPhysChem*, 2012, **13**, 3383-3387.

134. R. t. Shannon, *Acta Crystallographica Section A: Crystal Physics, Diffraction, Theoretical and General Crystallography*, 1976, **32**, 751-767.

135. T. Shimizu, J. Ueda and S. Tanabe, *physica status solidi (c)*, 2012, **9**, 2296-2299.

136. M. Reid, L. Van Pieterson, R. Wegh and A. Meijerink, *Physical Review B*, 2000, **62**, 14744.

137. P. Peijzel, P. Vergeer, A. Meijerink, M. Reid, L. Boatner and G. W. Burdick, *Physical Review B*, 2005, **71**, 045116.

138. L. Van Pieterson, M. Reid, R. Wegh, S. Soverna and A. Meijerink, *Physical Review B*, 2002, **65**, 045113.

139. H. Przybylińska, C.-G. Ma, M. Brik, A. Kamińska, P. Sybilski, A. Wittlin, M. Berkowski, Y. Zorenko, V. Gorbenko and H. Wrzesinski, *Applied physics letters*, 2013, **102**, 241112.

140. H. Przybylińska, C.-G. Ma, M. Brik, A. Kamińska, J. Szczepkowski, P. Sybilski, A. Wittlin, M. Berkowski, W. Jastrzębski and A. Suchocki, *Physical Review B*, 2013, **87**, 045114.

141. T. Tomiki, T. Kohatsu, H. Shimabukuro and Y. Ganaha, *Journal of the Physical Society of Japan*, 1992, **61**, 2382-2387.

142. Y. Pan, W. Wang, G. Liu, S. Skanthakumar, R. Rosenberg, X. Guo and K. K. Li, *Journal of Alloys and Compounds*, 2009, **488**, 638-642.

143. K. Ivanovskikh, J. Ogiegło, A. Zych, C. Ronda and A. Meijerink, *ECS journal of solid state science and technology*, 2013, **2**, R3148-R3152.

144. L. Seijo, Z. Barandiarán and E. Harguindey, *The Journal of Chemical Physics*, 2001, **114**, 118-129.

145. J. L. Pascual, N. Barros, Z. Barandiarán and L. Seijo, *The Journal of Physical Chemistry A*, 2009, **113**, 12454-12460.

146. M. Sekiya, T. Noro, E. Miyoshi, Y. Osanai and T. Koga, *Journal of computational chemistry*, 2006, **27**, 463-470.

147. O. Kazuyoshi, W. Shinta, S. Yuki, T. Hiroaki, I. Takugo, G. B. Mikhail and T. Isao, *Japanese Journal of Applied Physics*, 2004, **43**, L611.

148. K. Ogasawara, S. Watanabe, H. Toyoshima, T. Ishii, M. G. Brik, H. Ikeno and I. Tanaka, *J. Solid State Chem.*, 2005, **178**, 412-418.

149. Z.-x. Fang, L.-x. Ning and Z.-f. Cui, *Chinese Journal of Chemical Physics*, 2011, **24**, 134-140.

150. J. Gracia, L. Seijo, Z. Barandiarán, D. Curulla, H. Niemansverdriet and W. van Gennip, *Journal of Luminescence*, 2008, **128**, 1248-1254.

151. A. B. Muñoz-García, J. L. Pascual, Z. Barandiarán and L. Seijo, *Physical Review B*, 2010, **82**, 064114.

152. A. B. Muñoz-García and L. Seijo, *Physical Review B*, 2010, **82**, 184118.

153. L. Chen, X. Chen, F. Liu, H. Chen, H. Wang, E. Zhao, Y. Jiang, T.-S. Chan, C.-H. Wang and W. Zhang, *Scientific reports*, 2015, **5**.

154. Z. Xia and Q. Liu, *Prog. Mater Sci.*, 2016, **84**, 59-117.